Physica D 251 (2013) 39–59

Contents lists available at SciVerse ScienceDirect

Physica D

journal homepage: www.elsevier.com/locate/physd

Breathers in oscillator chains with Hertzian interactions

Guillaume James [a,*], Panayotis G. Kevrekidis [b], Jesús Cuevas [c]

[a] Laboratoire Jean Kuntzmann, Université de Grenoble and CNRS, BP 53, 38041 Grenoble Cedex 9, France

[b] Department of Mathematics and Statistics, University of Massachusetts, Amherst, MA 01003-4515, USA

[c] Grupo de Física No Lineal, Departamento de Física Aplicada I, Escuela Politécnica Superior, Universidad de Sevilla, C/ Virgen de África, 7. 41011 Sevilla, Spain

ARTICLE INFO

Article history:
Received 2 November 2011
Received in revised form
22 January 2013
Accepted 28 January 2013
Available online 13 February 2013
Communicated by B. Sandstede

Keywords:
Hamiltonian lattice
Hertzian contact
Discrete breather
Direction-reversing wave
Surface mode
Discrete *p*-Schrödinger equation

ABSTRACT

We prove nonexistence of breathers (spatially localized and time-periodic oscillations) for a class of Fermi–Pasta–Ulam lattices representing an uncompressed chain of beads interacting via Hertz's contact forces. We then consider the setting in which an additional on-site potential is present, motivated by the Newton's cradle under the effect of gravity. We show the existence of breathers in such systems, using both direct numerical computations and a simplified asymptotic model of the oscillator chain, the so-called discrete *p*-Schrödinger (DpS) equation. From a spectral analysis, we determine breather stability and explain their translational motion under very weak perturbations. Numerical simulations demonstrate the excitation of traveling breathers from simple initial conditions corresponding to small perturbations at the first site of the chain. This regime is well described by the DpS equation, and is found to occur for physical parameter values in granular chains with stiff local oscillators. In addition, traveling breather propagation can be hindered or even suppressed in other parameter regimes. For soft on-site potentials, a part of the energy remains trapped near the boundary and forms a surface mode. For hard on-site potentials and large to moderate initial excitations, one observes a "boomeron", i.e. a traveling breather displaying spontaneous direction-reversing motion. In addition, dispersion is significantly enhanced when a precompression is applied to the chain. Depending on parameters, this results either in the absence of traveling breather excitation on long time scales, or in the formation of a "nanopteron" characterized by a sizable wave train lying at both sides of the localized excitation.

1. Introduction

The study of nonlinear waves in granular crystals is the object of intensive research, both from a theoretical perspective and for practical purposes, e.g. for the design of shock absorbers [1,2], acoustic lenses [3] or diodes [4]. Due to the nonlinear interactions between grains, several interesting types of localized waves can be generated in chains of beads in contact. Solitary waves are the most studied type of excitations and can be easily generated by an impact at one end of a chain [5–9,1]. These solitary waves, in the absence of an original compression in the chain (the so-called precompression), differ from classical ones (i.e. KdV-type solitary waves [10]) due to the fully nonlinear character of Hertzian contact interactions. Indeed, their decay is super-exponential and their width remains unchanged with amplitude [11,12].

Another interesting class of excitations consists of time-periodic and spatially localized oscillations. Such waves may correspond to Anderson modes [13] in the presence of spatial disorder, or to defect modes localized at an impurity in a granular chain under precompression [14]. A different class of spatially localized oscillations that occur in the absence of defects consists of discrete breathers, which originate from the combined effects of nonlinearity and spatial discreteness (see the review [15]). These waves exist in diatomic granular chains under precompression [16–18], with their frequency lying between the acoustic and optic phonon bands and can be generated e.g. through modulational instabilities. However, because precompression suppresses the fully nonlinear character of Hertzian interactions, these excitations inherit the usual properties of discrete breathers, i.e. their spatial decay is exponential and their width diverges at vanishing amplitude, i.e. for frequencies close to the bottom of the optic band [18].

For granular systems without precompression, the above discussion raises the question of existence of spatially localized oscillations. Defect modes induced by a mass impurity have been numerically observed in unloaded granular chains [19,20], but these excitations were found to occur only on short transients. The existence of long-lived localized oscillations has been only reported for granular chains including on-site potentials in addition to the usual Hertzians interaction [21,22]. Models in this class describe e.g. the small amplitude waves in a classical Newton's cradle [23], which consists of a chain of beads attached to pendula

* Corresponding author.
E-mail address: guillaume.james@imag.fr (G. James).

0167-2789/$ – see front matter © 2013 Elsevier B.V. All rights reserved.
doi:10.1016/j.physd.2013.01.017

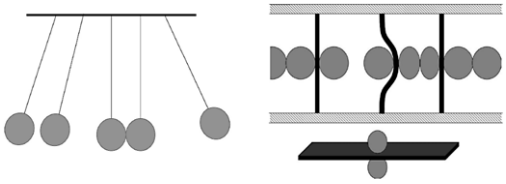

Fig. 1. Left: prototypical Newton's cradle. Right: stiff Newton's cradle, consisting of an array of clamped cantilevers decorated by spherical beads (displacements are amplified for clarity).

(see Fig. 1, left). In [21], static and moving breathers were numerically observed as a result of modulational instabilities of periodic traveling waves, and extremely stable static breathers were generated from specific initial conditions. In addition, a reduced model, the so-called discrete *p*-Schrödinger (DpS) equation was derived as an asymptotic model for small amplitude oscillations in the Newton's cradle, and successfully reproduced the above localization phenomena. The discrete breathers possess special properties both in the original cradle model and the simplified DpS system, i.e. their spatial decay is super-exponential and their width remains nearly constant at small amplitude.

In this paper we extend the above results in two directions.

Firstly, we prove in Section 2 the *nonexistence* of *time-periodic* spatially localized oscillations in uncompressed granular chains in the absence of local potentials. This result seems surprising at a first glance, because Hertzian models of granular chains fall within the class of Fermi–Pasta–Ulam (FPU) lattices, which sustain discrete breathers under some general assumptions on the interaction potentials and particle masses (see [24] and references therein). However these conditions do not hold for uncompressed granular chains. Using a simple averaging argument, we show that the non-attracting character of Hertzian interactions between grains (repulsive under contact, and vanishing in the absence of contact) precludes the existence of time-periodic localized oscillations, both for spatially homogeneous or inhomogeneous chains.

Our second contribution concerns the case of (generalized) Newton's cradles, i.e. spatially homogeneous granular chains incorporating a local harmonic or anharmonic potential (taking the form of an even quartic polynomial). We analyze the existence and qualitative properties of time-periodic and traveling breathers, and the possible excitation of traveling breathers from an impact at the end of a chain. We consider two different situations corresponding respectively to the absence or presence of a precompression of the chain, and yielding quite different dynamical behaviors. The case without precompression is examined in Section 3, where we obtain the following results.

1. In Section 3.2, we use a Newton method to compute branches of site- and bond-centered breathers parametrized by their frequency $\omega > \omega_0$ (ω_0 being the linear frequency of the local oscillators). These branches bifurcate from the trivial equilibrium when $\omega \to \omega_0$ (where analytical approximations of breather profiles are also obtained), and can be continued up to a strongly nonlinear regime. The spectral stability of these breather solutions is analyzed for some parameter values, and depends on the type (and strength) of the local anharmonicity. In addition, we observe a near-degeneracy in the spectrum (associated with a so-called "pinning mode" [25]), resulting in a transition from static to traveling breathers under very small perturbations.

   Having obtained traveling breathers from small perturbations of static ones, we study in Section 3.3 if they can arise from much simpler initial conditions, and attempt to excite the first site of a Newton's cradle.
2. In Section 3.3.1, we identify four different dynamical regimes depending on the parameter values (and time scales) considered. The first one corresponds to small initial excitations, and long (generally finite) time intervals on which the dynamics of Newton's cradle and the DpS equation are similar (this is in agreement with recent theoretical results of [26]). In this regime, the main stress wave takes the form of a traveling breather propagating almost freely along the chain. The second regime is obtained for harmonic on-site potentials in the limit of large amplitude perturbations, where soliton-like excitations are observed, a situation reminiscent of [5,7]. In the third regime, which occurs for soft on-site potentials and large to moderate initial excitations, a significant part of the energy does not propagate and remains trapped near the boundary (forming a so-called surface mode [27]), while a small amplitude traveling breather is generated. The last regime corresponds to hard on-site potentials and large to moderate initial excitations (or sufficiently long time scales). In that case, the initial perturbation produces a "boomeron" (direction-reversing traveling breather) reminiscent of excitations previously obtained in particular integrable models (see [28] and references therein).
3. In Section 3.3.2, we examine possible experimental realizations of these kinds of granular lattices and the related observation of moving breathers after an impact (i.e. an initial excitation of the first site of the chain). As it follows from the results of Section 3.3.1, the DpS regime giving rise to (almost) freely-propagating breathers is realized for small enough impact velocities. Combining this result with suitable scaling arguments, we deduce that moving breathers would not be observable in practice in a classical Newton's cradle acting under gravity. In addition, we argue that reasonably simple mechanical systems with stiff local oscillators could be tailored so that the DpS regime takes place. As a prototype for which this situation occurs, we consider the chain of identical clamped cantilevers represented in Fig. 1. Each cantilever is decorated by two spherical beads attached to its center, and the beads of two successive cantilevers are tangent at the ground state. Using a reduced oscillator chain model of this system (calibrated for realistic material parameter values), we check that an impact on the first cantilever generates indeed a moving breather.

Lastly, the case of a Newton's cradle under precompression is studied in Section 4. Since precompression adds effectively a linear component to Hertzian interactions, this system falls within a more standard class of models, the so-called mixed Klein–Gordon/Fermi–Pasta–Ulam lattices [29]. Traveling or static breathers close to envelope solitons of the (focusing) continuum nonlinear Schrödinger (NLS) equation exist in such systems, at least in the small amplitude limit and on long transients [30,31]. They can be easily generated from modulational instabilities, starting from "well-prepared" initial data leading to similar dynamics in the original lattice and the NLS equation. However, for a highly localized initial disturbance of the chain, such as the excitation of a single particle, no correspondence with the NLS equation has been mathematically established up to now. Whether traveling breathers may form or not after an impact is therefore a nontrivial theoretical problem. Another interesting question concerns the qualitative properties of the corresponding breathers (if they form), and in particular the differences compared to traveling breathers in uncompressed chains. In numerical simulations, we observe the formation of an important dispersive wave train and the generation or absence of a traveling breather depending on the local potential. Traveling breather propagation does not occur (at least on the timescale of the simulations) with our choice of harmonic and soft on-site potentials, a property that we (heuristically) relate to the growth rates of modes during modulational instability. A traveling breather is observed in the hard potential case, but is found much less localized than in the absence of precompression. In addition, the main pulse is sitting on a sizable non-decaying oscillatory tail extending at both sides,

the ensemble forming a so-called "nanopteron" [32]. According to our findings, the precompression introduces therefore a very different phenomenology (compared to the case of Section 3), where dispersion becomes much more dominant and different effects of the local anharmonicity are observed.

To conclude this paper, we state in Section 5 some relevant theoretical problems left open in this study, and discuss our results from a more general perspective in connection with possible experiments.

2. Nonexistence of breathers in FPU chains with repulsive interactions

We consider an infinite chain of particles of masses $m_n > 0$, interacting with their nearest neighbors via anharmonic potentials V_n. This type of system (which can be thought of in general, i.e., for unequal masses m_n, as a spatially inhomogeneous FPU lattice) corresponds to the Hamiltonian

$$\mathcal{H} = \sum_{n\in\mathbb{Z}} \frac{m_n}{2}\dot{x}_n^2 + V_n(x_{n+1} - x_n) \tag{1}$$

where x_n denotes the particle displacements from the ground state. We consider interaction potentials V_n of the form

$$V_n(x) = W_n[(-x)_+],$$

where $(a)_+ = \max(a, 0)$, $W_n \in C^1(\mathbb{R}^+, \mathbb{R}^+)$, $W_n'(0) = 0$ and $W_n'(x) > 0$ for all $x > 0$. The form of V_n implies that particle interactions are repulsive under compression (i.e. for $x < 0$) and unilateral (interaction forces vanish under extension, i.e. for $x > 0$).

Moreover we assume

$$W_n'(x) \le f(x) \quad \forall x \in [0, r],\ \forall n \ge n_0, \tag{2}$$

for some real constant $r > 0$, integer n_0 and a monotone increasing function $f \in C^0([0, r])$ satisfying $f(0) = 0$. For example, these assumptions are satisfied with $f(x) = \sup_{n\ge n_0} W_n'(x)$ if the functions W_n are convex in $[0, r]$ and belong to some finite set for $n \ge n_0$ (this is the case in particular for spatially periodic systems). Another example is given by Hertzian interactions

$$W_n(x) = \frac{1}{\alpha_n + 1}\gamma_n x^{\alpha_n+1},$$

where the coefficients $\gamma_n, \alpha_n > 0$ depend on material properties and particle geometry. In that case one can choose $f(x) = \gamma x^\alpha$ (and $r = 1$) provided $\gamma_n \le \gamma$ and $\alpha_n \ge \alpha > 0$ for all $n \ge n_0$.

The Hamiltonian (1) leads to the equations of motion

$$m_n\ddot{x}_n = V_n'(x_{n+1} - x_n) - V_{n-1}'(x_n - x_{n-1}), \quad n \in \mathbb{Z}. \tag{3}$$

In what follows we show that under the above assumptions, the only time-periodic breather solutions of (3) are trivial equilibria. Due to the translational invariance of (1), breathers are defined as time-periodic solutions which converge (uniformly in time) towards translations $x_n = c_\pm \in \mathbb{R}$ as $n \to \pm\infty$. This implies that relative particle displacements vanish at infinity, i.e. one has

$$\lim_{n\to\pm\infty} \|x_n - x_{n-1}\|_{L^\infty(0,T)} = 0 \tag{4}$$

for a T-periodic breather. In what follows, we prove in fact a more general nonexistence result of nontrivial periodic solutions vanishing as $n \to +\infty$.

Theorem 1. *All time-periodic solutions of (3) satisfying*

$$\lim_{n\to+\infty} \|x_n - x_{n-1}\|_{L^\infty} = 0 \tag{5}$$

are independent of t and increasing with respect to n.

Proof. Let us consider a T-periodic solution of (3) and integrate (3) over one period. This yields the equality

$$\bar{F}_n = \bar{F}_{n+1},$$

where $\bar{F}_n = \frac{1}{T}\int_0^T V_{n-1}'(x_n(t) - x_{n-1}(t))\,dt$ is the average interaction force between masses $n-1$ and n. Consequently $\bar{F}_n = \bar{F}$ is independent of n.

Now let us check that $\bar{F}$ vanishes thanks to the bound (2) uniform in n. We have for all n

$$\begin{aligned}|\bar{F}| &= \frac{1}{T}\int_0^T W_{n-1}'[(x_{n-1}(t) - x_n(t))_+]\,dt \\ &\le \|W_{n-1}'[(x_{n-1} - x_n)_+]\|_{L^\infty}.\end{aligned}$$

Taking into account (5) and (2), the above inequality yields for n large enough

$$|\bar{F}| \le \|f[(x_{n-1} - x_n)_+]\|_{L^\infty} = f[\|(x_{n-1} - x_n)_+\|_{L^\infty}]$$

since f is increasing. It follows that

$$|\bar{F}| \le f(\|x_{n-1} - x_n\|_{L^\infty}) \to 0 \quad \text{as } n \to +\infty$$

hence $\bar{F} = 0$.

Now we use the fact that the interactions between particles are repulsive, i.e. we have $-V_n'(x) = W_n'[(-x)_+] \ge 0$. Since the T-periodic functions $F_n(t) = V_{n-1}'(x_n(t) - x_{n-1}(t))$ are negative, continuous and satisfy $\int_0^T F_n(t)\,dt = 0$ as shown previously, we have consequently $F_n(t) = 0$ for all t and n. Using (3), this implies $\ddot{x}_n = 0$ and thus x_n is an equilibrium solution (due to time-periodicity). Moreover one has $x_n \ge x_{n-1}$ since $F_n = 0$. □

We note that the above arguments do not work if an on-site potential is added to (1), because the average interaction forces are no more independent of n. In the next section, we numerically show the existence of breathers for such type of nonlinear lattices.

3. Breathers in uncompressed granular chains with local potentials

3.1. Models and methods

In this section we consider an extension of the Hertzian chain (1) incorporating local potentials. We analyze the existence and qualitative properties of time-periodic and traveling breathers (Section 3.2), and illustrate how to excite traveling breathers from simple initial conditions (Section 3.3). Our approach is based both on numerical and asymptotic methods.

In Section 3.2.1, the modified Gauss–Newton method introduced in [33] is used to compute branches of breather solutions bifurcating from the ground state. Their spectral stability is investigated in Section 3.2.2, in relation with their translational motion under perturbations. More precisely, their Floquet spectra display (in addition to the usual double eigenvalue $+1$) an extra pair of eigenvalues very close to unity. As an effect of this near-degeneracy, we show that small perturbations of the breathers along an associated pinning mode generate a translational motion with negligible radiation, according to the process analyzed in [25]. In addition, the concept of Peierls–Nabarro barrier [34,35] allows one to approximate the amount of energy required for the depinning of stable breathers.

In addition to the direct approach described above, the main qualitative properties of small amplitude breathers are also captured from the asymptotic limit of the DpS equation. In particular, we derive quasi-continuum approximations of the breather profiles valid at small amplitude. These approximate breathers have a compact support, which provides a reasonable approximation to

the super-exponential decay of the exact breathers (in analogy to what is known for the approximation of solitons in uncompressed granular chains [5,11]).

Having observed the mobility of static breathers under small perturbations in Section 3.2, we explore in Section 3.3 the excitation of traveling breathers from a velocity perturbation at the end of a semi-infinite chain. In Section 3.3.1, we show the relevance of the DpS equation for describing (over long finite times) the traveling breather propagation after a small amplitude initial perturbation. In addition, we show the failure of the DpS equation for capturing new types of waves (surface modes and boomerons) showing up for anharmonic local potentials and (mainly) for larger perturbations. In Section 3.3.2, we argue that the traveling breather excitations obtained in Section 3.3.1 are relevant in the context of impact mechanics, i.e. can be obtained in granular chains with local potentials for realistic parameter values.

3.1.1. Hertzian granular chains with on-site potentials

We consider a nonlinear lattice with the Hamiltonian

$$\mathcal{H} = \sum_n \frac{1}{2}\dot{y}_n^2 + W(y_n) + V(y_{n+1} - y_n), \tag{6}$$

where

$$V(r) = \frac{2}{5}(-r)_+^{5/2}. \tag{7}$$

The system (6) corresponds to a chain of identical particles in the local potential W, coupled by the classical Hertz potential V describing contacts between smooth non-conforming surfaces. Unless explicitly stated, the on-site potential W will be chosen harmonic with

$$W(y) = \frac{1}{2}y^2. \tag{8}$$

In that case, the dynamical equations read

$$\ddot{y}_n + y_n = (y_{n-1} - y_n)_+^{3/2} - (y_n - y_{n+1})_+^{3/2}. \tag{9}$$

Fig. 1 depicts two examples of such systems. In practical situations, the assumption of a local harmonic potential implies that the model will be valid for small amplitude waves and suitable time scales on which higher order terms can be neglected. In order to capture higher order effects, different parts of our analysis will be extended to symmetric anharmonic local potentials

$$W(y) = \frac{1}{2}y^2 + \frac{s}{4}y^4, \tag{10}$$

where the parameter s measures the degree of anharmonicity.

In the work [21], long-lived static and traveling breather solutions of (9) have been numerically observed, starting from suitably chosen localized initial conditions, or from small perturbations of unstable periodic traveling waves. However, the classical result of MacKay and Aubry [36] proving the existence of static breathers near the anti-continuum limit does not apply in that case. Indeed, if Hertzian interactions forces are canceled (or equivalently, if one considers breathers in the limit of vanishing amplitude), one obtains an infinite lattice of identical linear oscillators, and the nonresonance assumption of Ref. [36] is not satisfied. The anti-continuum limit can be only used for models incorporating anharmonic on-site potentials, and under the assumption of weak Hertzian interactions whose applicability is rather limited [37]. Moreover, other existence proofs based on spatial dynamics and the center manifold theorem [38] do not apply, due to the fully-nonlinear character of interaction forces (the same remark holds true in the case of traveling breathers [39]). Variational tools [24] may be suitable to obtain existence proofs in this context, but this question is outside the scope of the present paper, where we chiefly resort to numerical and asymptotic methods.

In the following section, we recall the relation between (9) and the asymptotic model given by the DpS equation [21].

3.1.2. The discrete p-Schrödinger limit

Small amplitude solutions of system (6)–(8) can be well approximated by an equation of the nonlinear Schrödinger type, namely the discrete p-Schrödinger (DpS) equation with $p = 5/2$

$$i\dot{v}_n = (v_{n+1} - v_n)|v_{n+1} - v_n|^{p-2} - (v_n - v_{n-1})|v_n - v_{n-1}|^{p-2}. \tag{11}$$

The most standard model reminiscent of this family of equations is the so-called discrete nonlinear Schrödinger (DNLS) equation, studied in detail in a number of different contexts, including nonlinear optics and atomic physics over the past decade [40]. However, the DpS equation is fundamentally different in that it contains a fully nonlinear inter-site coupling term, corresponding to a discrete p-Laplacian.

To make the connection with the DpS equation more precise, we sum up some basic elements of the analysis of [21]. Let us consider the lattice model (9) and the DpS equation

$$2i\tau_0\dot{A}_n = (A_{n+1} - A_n)|A_{n+1} - A_n|^{1/2} - (A_n - A_{n-1})\,|A_n - A_{n-1}|^{1/2}, \tag{12}$$

where $\tau_0 = \frac{5(\Gamma(\frac{1}{4}))^2}{24\sqrt{\pi}} \approx 1.545$ and Γ denotes Euler's Gamma function. Given a solution of (12) and $\epsilon > 0$ small enough, one obtains an approximate solution of (9)

$$y_n^{\mathrm{app}}(t) = 2\epsilon\ \mathrm{Re}[A_n(\epsilon^{1/2}t)\ e^{it}]. \tag{13}$$

The approximate solution (13) and amplitude Eq. (12) have been derived in [21] using a multiple-scale expansion. According to [26], for initial conditions of the form $y_n(0) = 2\epsilon\ \mathrm{Re}\,[A_n(0)] + O(\epsilon^{3/2})$, $\dot{y}_n(0) = -2\,\epsilon\,\mathrm{Im}\,[A_n(0)] + O(\epsilon^{3/2})$ with $\epsilon \approx 0$, this approximation is $O(\epsilon^{3/2})$-close to the exact solution of (9) at least up to times $t = O(\epsilon^{-1/2})$ (see also numerical results of [21] comparing the DpS approximation and exact solutions of (9)). Moreover, for some family of periodic traveling wave solutions of the DpS equation, the ansatz (13) is $O(\epsilon^{3/2})$-close to exact small amplitude periodic traveling waves of (9) [21].

Lastly, it is interesting to mention that the DpS equation depends on the terms of (9) up to order $O(|y|^{3/2})$ (see [21], section 2.1). It follows that this equation remains unchanged for smooth anharmonic on-site potentials $W(y) = \frac{1}{2}y^2 + O(|y|^3)$, because the associated extra nonlinearity is at least quadratic. Consequently, the addition of a local anharmonicity does not change the dynamics of (9) for small amplitude waves, on the time scales governed by the DpS equation.

3.2. Existence and properties of static and traveling breathers

3.2.1. Bifurcations of static breathers from the ground state

The work of [21] illustrated the existence of time-periodic and spatially localized solutions of the DpS equation. Figs. 2 and 3 (top left panels) display the profiles of spatially antisymmetric or symmetric breather solutions of the DpS Eq. (11). These are sought by using the standard stationary ansatz for DNLS type equations of the form $v_n = \exp(i\mu t)\,u_n$ with $\mu > 0$ and $u_n \in \mathbb{R}$. The resulting coupled nonlinear algebraic equations read

$$-\mu u_n = (u_{n+1} - u_n)|u_{n+1} - u_n|^{1/2} - (u_n - u_{n-1})|u_n - u_{n-1}|^{1/2} \tag{14}$$

and are solved via a fixed point iteration of the Newton–Raphson type, for free end boundary conditions (Eq. (14) is considered for $n = 1, \ldots, N$ with $u_0 \stackrel{\mathrm{def}}{=} u_1$ and $u_{N+1} \stackrel{\mathrm{def}}{=} u_N$).

Note that Eq. (11) has a scale invariance, since any solution $v_n(t)$ generates a one-parameter family of solutions $a\,v_n(|a|^{1/2}\,t)$,

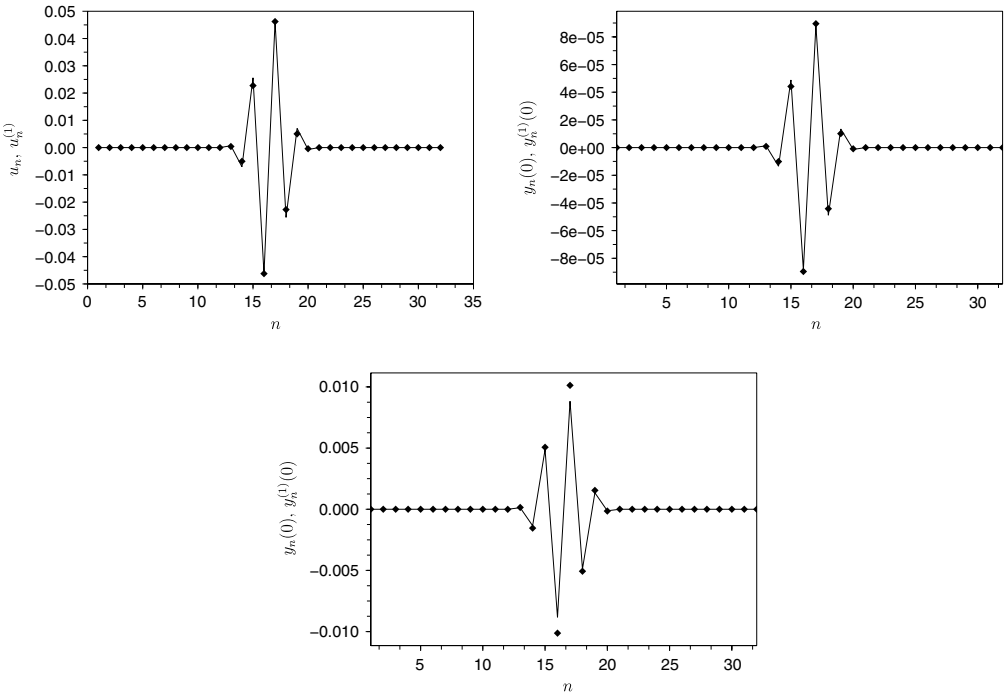

Fig. 2. Top left panel: spatially antisymmetric solution u_n of the stationary DpS Eq. (14), computed numerically for $\mu = 1$ (marks). This solution is compared to the quasi-continuum approximation $u_n^{(1)}$ defined by Eq. (18) (continuous line). The other graphs compare a bond-centered breather y_n solution of (9) computed numerically (marks) and its quasi-continuum approximation $y_n^{(1)}$ (continuous line). The top right plot corresponds to a small amplitude breather ($\omega_b = 1.01$), and the bottom plot to a more strongly nonlinear regime ($\omega_b = 1.1$). Particle positions are plotted at the instant of maximal amplitude.

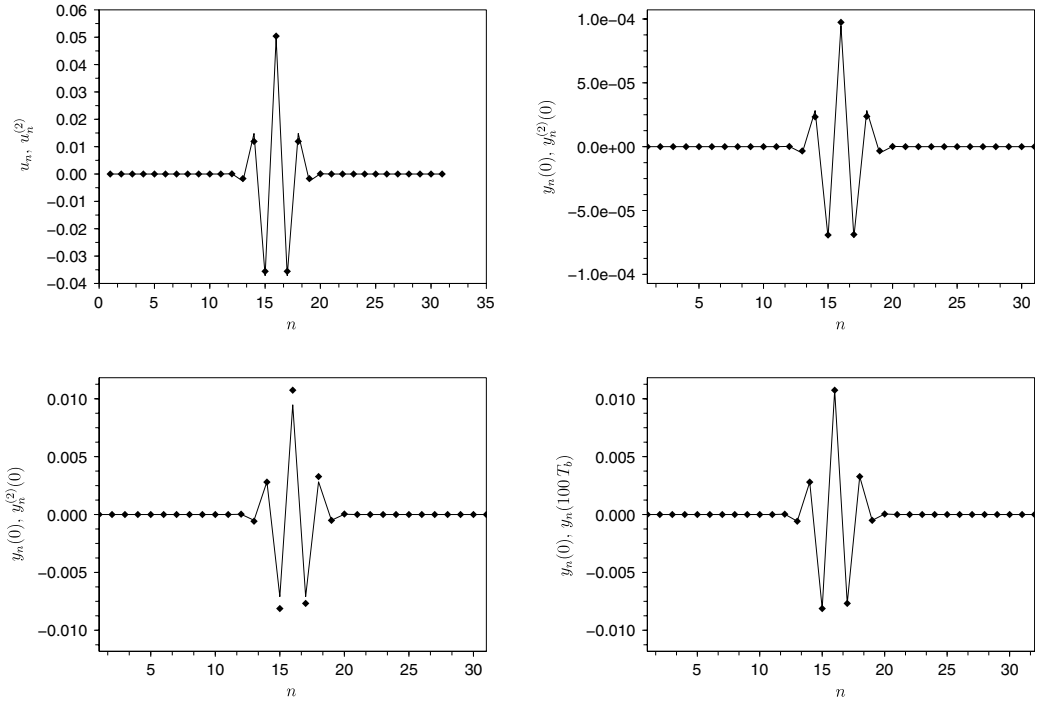

Fig. 3. Top left panel: spatially symmetric solution u_n of the stationary DpS Eq. (14), computed numerically for $\mu = 1$ (marks). This solution is compared to the quasi-continuum approximation $u_n^{(2)}$ defined by Eq. (19) (continuous line). Top right panel: small amplitude site-centered breather y_n solution of (9) computed numerically for $\omega_b = 1.01$ (marks) and its quasi-continuum approximation $y_n^{(2)}$ (continuous line). Particle positions are plotted at the instant of maximal amplitude. Bottom left panel: same computation for $\omega_b = 1.1$, corresponding to a more strongly nonlinear regime. In the bottom right plot, the breather computed numerically for $\omega_b = 1.1$ is compared to its evolution at $t = 100\,T_b$ (marks).

$a \in \mathbb{R}$. Thanks to this scale invariance, the whole families of antisymmetric and symmetric breathers can be reconstructed from the case $\mu = 1$ of (14). In particular, breather amplitudes are $\propto \mu^2$ and the breather width remains unchanged when $\mu \to 0$, a property that strongly differs from the broadening of DNLS breathers at small amplitude (see e.g. [41], Section 3).

In what follows we approach the two breather profiles using a quasi-continuum approximation. Fixing $\mu = 1$ and introducing

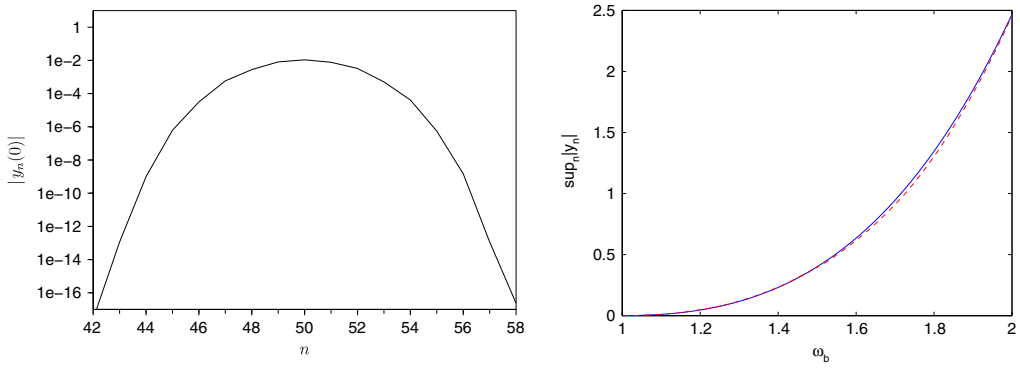

Fig. 4. Left plot: moduli of the initial breather positions computed by the Newton method, plotted in semi-logarithmic scale. Computations are performed for a chain of 99 particles and a site-centered breather with frequency $\omega_b = 1.1$. Right plot: maximal amplitude at $t = 0$ of breather solutions of (9) as a function of their frequency ω_b. The continuous line corresponds to bond-centered breathers, and the dashed line to site-centered breathers (note that the two graphs are very close).

$w_n = (u_{n+1} - u_n)|u_{n+1} - u_n|^{1/2}$, Eq. (14) becomes

$$w_{n+1} - 2w_n + w_{n-1} + w_n|w_n|^{-1/3} = 0, \tag{15}$$

where the nonlinear coupling has been linearized (at the expense of having an on-site nonlinearity non-differentiable at the origin). The spatial profiles of Figs. 2 and 3 suggest to use the so-called staggering transformation $w_n = (-1)^n f(n)$, which yields

$$f(n+1) - 2f(n) + f(n-1) = -4f(n) + f(n)|f(n)|^{-1/3}. \tag{16}$$

Now we look for an *approximate* solution F of (16). For this purpose we use the formal approximation $F(n \pm 1) \approx F(n) \pm F'(n) + \frac{1}{2}F''(n)$, in same the spirit as the approximations of soliton profiles performed in Ref. [5] (the accuracy of this approximation will be checked a posteriori by numerical computations).[1] This leads to the differential equation

$$F'' = -4F + F|F|^{-1/3}, \tag{17}$$

which possesses a family of compactly supported solutions $F(x) = \pm g(x + \phi)$, where

$$g(x) = \left(\frac{3}{10}\right)^3 \cos^6\left(\frac{x}{3}\right) \quad \text{for } |x| \le \frac{3\pi}{2},\ g = 0 \text{ elsewhere.}$$

Replacing f by its approximation F and performing appropriate choices of sign and spatial shifts in F, one obtains the symmetric approximate solutions of (15)

$$w_n^{(1)} = (-1)^{n+1} g(n), \qquad w_n^{(2)} = (-1)^{n+1} g\left(n + \frac{1}{2}\right).$$

The case $\mu = 1$ of (14) yields $u_n = w_{n-1} - w_n$, therefore we get the following quasi-continuum approximations of the antisymmetric and symmetric breather profiles

$$u_n^{(1)} = (-1)^n \left[g(n) + g(n-1)\right], \tag{18}$$

$$u_n^{(2)} = (-1)^n \left[g\left(n + \frac{1}{2}\right) + g\left(n - \frac{1}{2}\right)\right]. \tag{19}$$

The first graphs of Figs. 2 and 3 show the excellent agreement of these approximations with the numerical solutions of the stationary DpS equation. Returning to the ansatz (13) and the time-dependent (non-renormalized) DpS Eq. (12), we obtain approximate breather solutions of (9) taking the form

$$y_n^{(s)}(t) = 2\epsilon\, u_n^{(s)} \cos(\omega_b t), \qquad \omega_b = 1 + \frac{\epsilon^{1/2}}{2\tau_0}, \quad s = 1, 2. \tag{20}$$

It is interesting to observe that approximation (20) is unaffected by smooth on-site nonlinear terms for $\epsilon \approx 0$, since we have noticed that the DpS equation remains unchanged.

In what follows we compare the above approximations with breather solutions of (9) computed numerically for free end boundary conditions (Eq. (9) is considered for $n = 1, \ldots, N$ with $y_0 \stackrel{\text{def}}{=} y_1$ and $y_{N+1} \stackrel{\text{def}}{=} y_N$). According to the approximate form (20), we expect to obtain families of site- and bond-centered solutions bifurcating from the ground state when $\omega \to 1^+$.

Let us denote $Y_n = (y_n, \dot{y}_n)$. We use an adapted Gauss–Newton method described in [33] to compute zeros $Y_n(0) = (y_n(0), 0)$ of the time-T_b map of the flow of (9), where $T_b = \frac{2\pi}{\omega_b}$ denotes the breather period. These initial conditions correspond to breathers even in time. An example of computation of a breather with frequency $\omega_b = 1.1$ is shown in Fig. 3 (the initial guess used for the Newton method is the site-centered approximate breather solution derived from the DpS equation). The bottom right panel of Fig. 3 compares the initial breather positions computed by the Newton method and their evolution at $t = 100\, T_b$, which shows that the breather oscillations are extremely stable. The super-exponential spatial decay of the breather is shown in Fig. 4 (see [37] for a recent analytical proof).

Using the above numerical scheme and path-following, we compute branches of breather solutions parametrized by their frequency $\omega_b > 1$. At the end of the Newton iteration, we get a relative residual error

$$\epsilon_{\text{res}} = \frac{\|\{Y_n(T_b) - Y_n(0)\}_n\|_\infty}{\|\{Y_n(0)\}_n\|_\infty} \sim 10^{-11},$$

and an incremental error

$$\epsilon_{\text{inc}} = \frac{\|\{y_n^{(k+1)}(0) - y_n^{(k)}(0)\}_n\|_\infty}{\|\{y_n^{(k+1)}(0)\}_n\|_\infty} \sim 10^{-8}$$

corresponding to the relative variation of particle positions between the k-th and $(k+1)$-th Newton iterates.

We obtain two branches of breather solutions of (9) with different symmetries. They consist of bond-centered breathers, i.e. spatially antisymmetric solutions satisfying $y_{-n+1} = -y_n$ (Fig. 2) and site-centered breathers (Fig. 3). The latter possess subtle symmetry properties. Since the Hertz potential is non-even, Eq. (9) is not invariant by the symmetry $Sy_n := y_{-n}$. However, the set of T_b-periodic solutions of (9) is invariant under the transformation $S'y_n(t) = -y_{-n}(t + T_b/2)$. The site-centered breathers of (9) are left invariant by S' and not by S (their asymmetry under S increases with ω_b, as shown in Fig. 3). In contrast, the DpS equation admits both symmetries S and S', which both leave the site-centered DpS breathers invariant. These different types of symmetries are illustrated by Figs. 2 and 3,

[1] Note that w_n corresponds to a spatially modulated binary oscillation, and a continuum approximation is obtained for its envelope, whereas the continuum approximation of [5] was performed on the full soliton profiles.

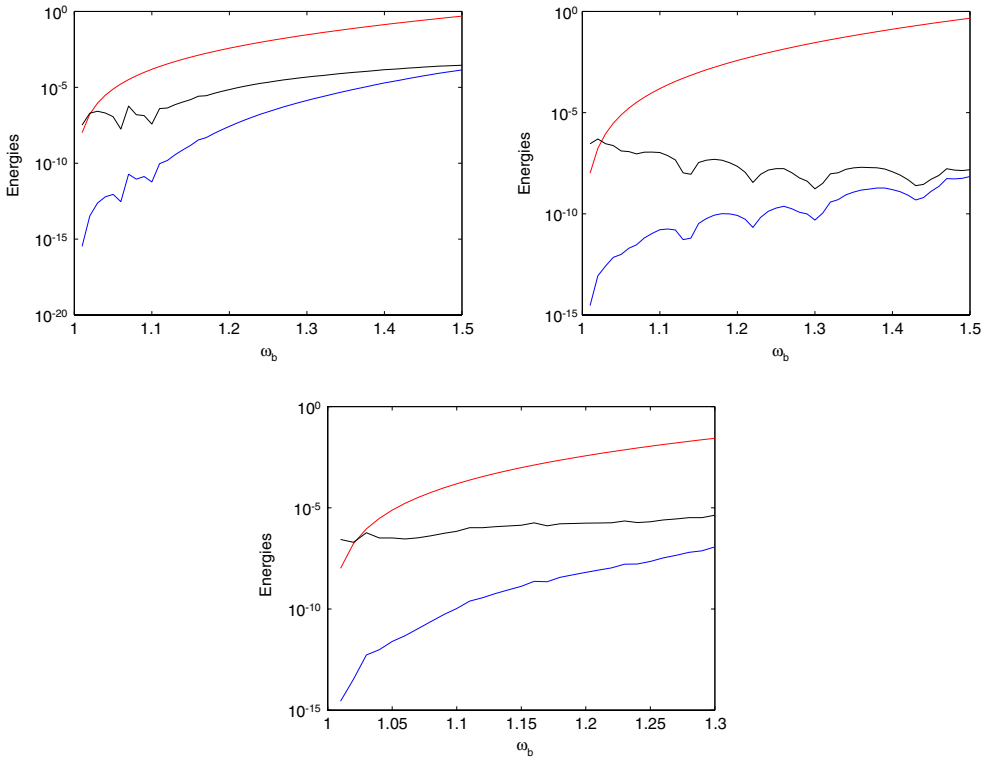

Fig. 5. Approximate Peierls–Nabarro barrier computed as a function of breather frequency, for different degrees of anharmonicity of the on-site potential (top left plot: $s = -1/6$, top right plot: $s = 0$, bottom plot: $s = 1$). The red curves give the energy E_{bc} of bond-centered breathers defined by (6). The blue curves correspond to the approximate Peierls–Nabarro barriers E_{PN} (see text), and the black curve to the relative energy ratio E_{PN}/E_{bc} between the energy barrier and the bond-centered breather energy. (For interpretation of the references to colour in this figure legend, the reader is referred to the web version of this article.)

which compare the approximations (20) with breather solutions of (9) computed by the Newton method. While approximation (20) is excellent at small amplitude (case $\omega_b = 1.01$), its accuracy deteriorates in a more strongly nonlinear regime (case $\omega_b = 1.1$).

More details on the continuation of discrete breathers in ω_b are shown in Fig. 4 (right panel), which compares the maximal amplitude of the bond-centered and site-centered breather solutions of (9) when ω_b is varied (the continuation is performed for $\omega_b \in (1, 2]$). Both solutions bifurcate from $y_n = 0$ when $\omega_b \to 1^+$, and their amplitude increases with ω_b.

More generally, considering system (6) with the local anharmonic potential (10) and choosing $s \in [-1, 1]$, we obtain branches of site-centered and bond-centered breathers bifurcating from the origin when $\omega_b \to 1^+$ (results not shown). The persistence of both types of symmetries is due to the evenness of W.

In what follows we study in more detail the energy barrier separating site-centered and bond-centered breathers. As illustrated below in Section 3.2.2, this allows us to approximate the so-called Peierls–Nabarro energy barrier, which corresponds to the amount of energy required to put a stable static breather into motion under a momentum perturbation.

A notion of energy barrier separating discrete breathers is usually defined as follows (cf. also [35]). From (18)–(20), one can deduce a family of *approximate* static breather solutions of (6)–(10)

$$y_n(t) = 2\epsilon \left[g\left(n + \frac{1}{2} - Q\right) + g\left(n - \frac{1}{2} - Q\right) \right] \times (-1)^n \cos(\omega_b t), \tag{21}$$

where $\omega_b = 1 + \frac{\epsilon^{1/2}}{2\tau_0}$ and $Q \in \mathbb{R}$ (the cases $Q = 0$ and $Q = 1/2$ corresponding respectively to site-centered and bond-centered breathers). According to the work of [35], approximate traveling breather solutions of (6)–(10) can be obtained from (21). Their dynamics is described by an effective Hamiltonian, whose critical points correspond to site-centered and bond-centered breathers having the same area $\mathcal{A} = \int_0^{T_b} \sum_n \dot{y}_n^2 \, dt$. The absolute energy difference $\tilde{E}_{PN}$ between the two breather solutions provides an approximation of the Peierls–Nabarro barrier. However, because the latter appears to be very small in system (6)–(10) (a phenomenon that will be illustrated in Section 3.2.2), its evaluation requires a very precise computation of breather solutions. The definition of $\tilde{E}_{PN}$ yields additional numerical difficulties, due to the fact that the two breather frequencies have to be retrieved from a given area $\mathcal{A}$. Due to these difficulties, we shall use a more straightforward approach. We define (following Ref. [34]) the approximate Peierls–Nabarro barrier $E_{PN} = |E_{sc} - E_{bc}|$ as the absolute difference between the energies E_{sc}, E_{bc} of site- and bond-centered breathers having the same frequency.

We obtain extremely small values of E_{PN} both for harmonic and anharmonic on-site potentials, even quite far from the small amplitude regime. This result is illustrated by Fig. 5 for $s = -1/6$, $s = 0$ and $s = 1$. For small amplitude breathers ($\omega_b \approx 1.01$ in our computations), the different values of s yield comparable values of E_{PN}, of the order of $10^{-14} - 10^{-15}$. We find that E_{PN} increases with the breather amplitude but remains very small in our parameter range (e.g. E_{PN} is close to 10^{-4} for $\omega_b = 1.5$ and $s = -1/6$). The harmonic case yields even much smaller barriers (by 3–4 orders of magnitude for $\omega_b = 1.3$). As shown by Fig. 5, the smaller relative energy difference between site-centered and bond-centered breathers is also achieved in the harmonic case.

In order to correctly interpret the results of Fig. 5, we should stress that our computation of E_{PN} yields sometimes only a rough approximation, but captures nevertheless the correct orders of magnitude (which is our objective here, since the above definition of E_{PN} provides itself only an approximation of the true Peierls–Nabarro barrier). This originates from the finite precision

of the breather computation and the very small values of the energy ratio E_{PN}/E_{bc} (or equivalently E_{PN}/E_{sc}) that we obtain. If one approximates the numerical error on breather positions by the incremental error ϵ_{inc}, then the relative error made on E_{PN} is of order $\epsilon_{\text{inc}}\, E_{bc}/E_{PN}$. Since we get $\epsilon_{\text{inc}} \sim 10^{-8}$, the relative error on E_{PN} is of order unity in the worst case of Fig. 5 ($s = 0$, $\omega_b = 1.5$).

The above results indicate that extremely small perturbations of the breathers are capable of putting them into motion (even more critically for harmonic on-site potentials), a phenomenon that will be illustrated in the next section.

3.2.2. Breather stability and mobility

In this section we examine the stability properties of spatially antisymmetric and symmetric breather solutions of (11) and (6), and link these properties with the existence of traveling breather solutions. The linear (spectral) stability of breather solutions of (11) is investigated by means of the perturbation [40]:

$$v_n(t) = \exp(i\mu t)\left[u_n + \left(a_n \exp(\lambda t) + b_n^{\star} \exp(\lambda^{\star} t)\right)\right] \tag{22}$$

where u_n is a spatially symmetric or antisymmetric solution of (14) homoclinic to 0. The resulting linear problem for the eigenvalue λ and the eigenvector $(a_n, b_n)^T$ (where ^{T} denotes transpose) is solved by standard numerical linear algebra solvers and the results are depicted by means of the spectral plane (λ_r, λ_i) of the eigenvalues $\lambda = \lambda_r + i\lambda_i$. Note that in this Hamiltonian system, whenever λ is an eigenvalue, so are $\lambda^{\star}$, $-\lambda$ and $-\lambda^{\star}$. In addition, the breather stability properties remain qualitatively unchanged for all values of μ. This follows from the scale invariance of (11) pointed out in Section 3.2.1, which also implies the linear dependence of the eigenvalues λ on μ. However, we note in passing that this simplification is obviously not valid for the model (9).

From the bottom panels of Fig. 6, we can infer that spatially antisymmetric solutions are spectrally stable (due to the absence of eigenvalues of non-vanishing real part) and therefore should be structurally robust, a result confirmed by our direct numerical simulations (data not shown here).

On the other hand, the stability and associated dynamical properties are more interesting in the case of the site-centered solution of Fig. 7. In this case, we can observe the presence of a real eigenvalue pair. As can be seen in the bottom panel of Fig. 7, the real part of the relevant eigenvalue pair (which corresponds to the instability growth rate) grows linearly with the eigenvalue parameter μ, inducing a progressively stronger instability for larger amplitude solutions. The dynamical manifestation of this instability is illustrated in Fig. 8. Here we perturb the dynamically unstable solution of the right panel of Fig. 7 by a uniformly distributed random perturbation (of amplitude 0.01). The projection of this random field on the unstable eigenvector of the site centered mode excites the manifestation of the dynamical instability of this mode which is, in turn, illustrated in the space–time evolution (where the colorbar corresponds to the field $|v_n(t)|^2$) of Fig. 8. Clearly, the instability of the site-centered mode is associated with a "translational" eigenmode of the linearization problem, whose excitation induces the motion of the localized mode.

Having determined the spectral stability of bond-centered and site-centered breather solutions in the DpS equation, we now consider the same problem for their analogues in the original lattice (6), including in our analysis the effect of a possible addition of a local anharmonic potential (10).

We have computed the Floquet spectrum of (6)–(10) linearized at the bond-centered breather and the site-centered breather, for different values of the breather frequency $\omega_b \in (1, 2]$ and the anharmonicity parameter $s \in [-1, 1]$. The Floquet spectrum includes a quadruplet of eigenvalues close to $+1$ and eigenvalues on the unit circle accumulating near $e^{\pm i2\pi/\omega_b}$. The spectral properties of these discrete breathers differ from usual ones [42] for several reasons.

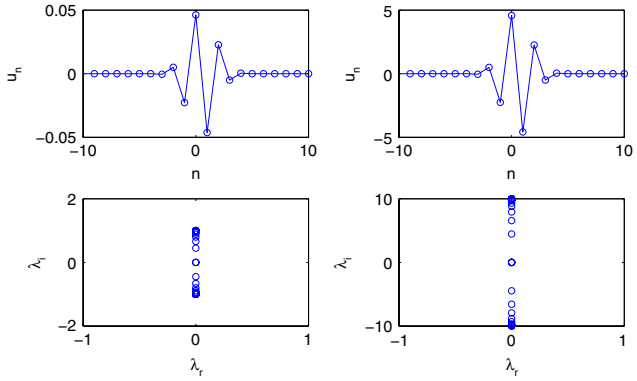

Fig. 6. The profiles (top panels) and the linear stability (bottom panels) of the spatially antisymmetric solution of the DpS equation are shown for the values of $\mu = 1$ (left panels) and $\mu = 10$ (right panels). This inter-site solution is linearly stable.

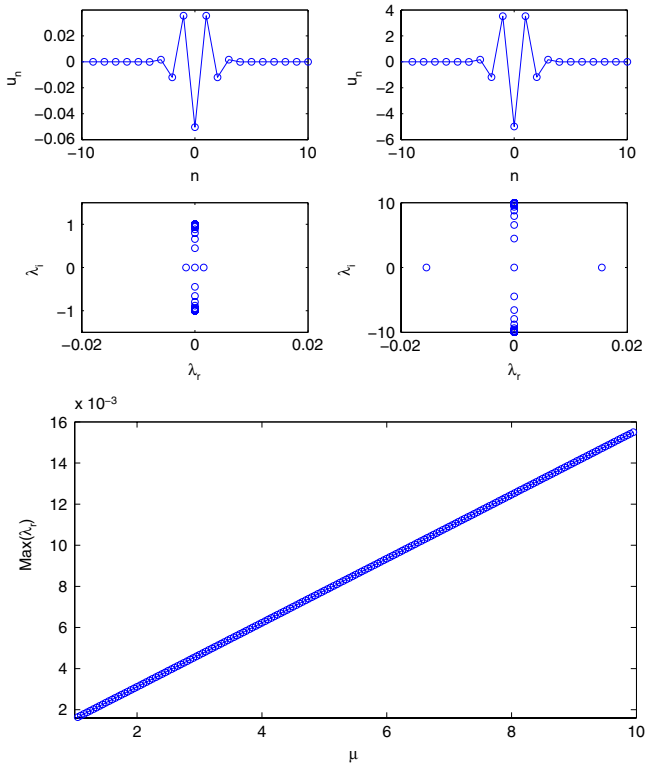

Fig. 7. The top two panels are directly analogous to the results of Fig. 6, but for the case of the site-centered solution. The presence of a (rather small) real eigenvalue pair of linearly growing magnitude as μ increases can be observed in the spectral plane and is more clearly highlighted in the figure of the bottom panel.

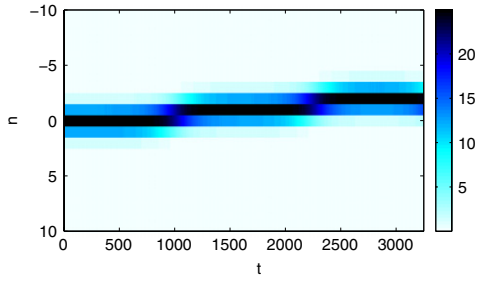

Fig. 8. The figure shows the space–time contour plot of the square modulus of the field $|v_n(t)|^2$ for Eq. (11). The initial condition is a site-centered localized mode (from the right column of Fig. 7), perturbed by a uniformly distributed random perturbation of amplitude 0.01. The perturbation leads to the manifestation of the instability of the site-centered mode which, in turn, leads to its mobility.

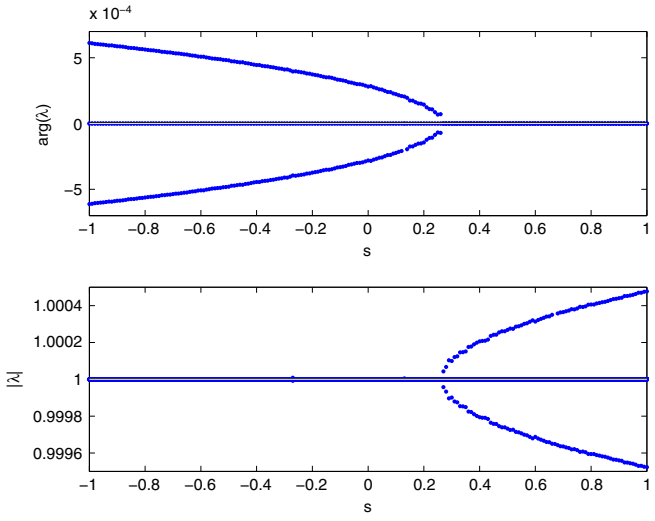

Fig. 9. Arguments (upper plot) and moduli (lower plot) of the quadruplet of Floquet eigenvalues λ close to $+1$, corresponding to system (9)–(10) linearized at the bond-centered breather. Computations are performed for $\omega_b = 1.1$, and eigenvalues are plotted as a function of the anharmonicity parameter $s \in [-1, 1]$.

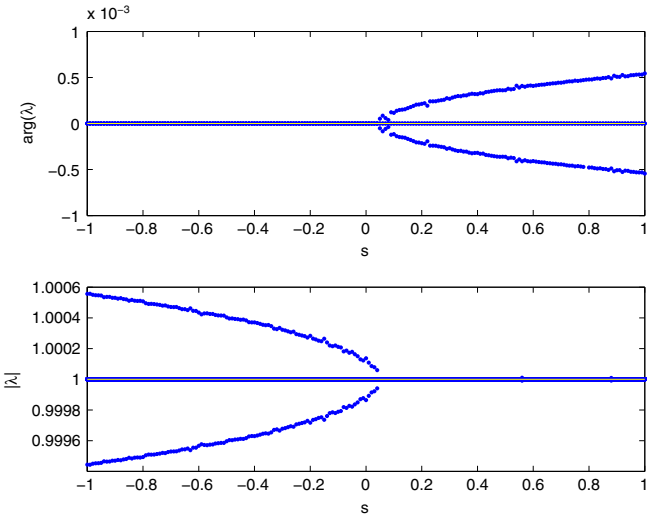

Fig. 10. Same plot as in Fig. 9, for the site-centered breather with $\omega_b = 1.1$.

Firstly, no bands of continuous spectrum are present on the unit circle for the infinite chain. This is due to the fact that system (9) linearized at $y_n = 0$ (the limit of a breather solution at infinity) consists of an infinite chain of uncoupled identical linear oscillators, and thus the phonon band reduces to a single frequency, equal to unity in the present case. Secondly, another nonstandard property originates from the quadruplet of eigenvalues close to $+1$. Due to the Hamiltonian character of (9), $+1$ is always at least a double eigenvalue of the Floquet matrix. In addition, we always find an extra pair of eigenvalues in the immediate vicinity of $+1$ corresponding to a pinning mode (see below). This contrasts with the case of Klein–Gordon lattices, where this situation is a codimension-one phenomenon, occurring near critical values of the coupling constant and for particular classes of on-site potentials [25,43].

In what follows we describe the evolution of the quadruplet of eigenvalues close to $+1$ for $\omega_b = 1.1$ and $s \in [-1, 1]$. The following figures display the moduli and arguments of these eigenvalues for the bond-centered breather (Fig. 9) and the site-centered breather (Fig. 10). For the bond-centered breather, a pair of Floquet multipliers λ, λ^{-1} emerges from the unit circle after a collision at $+1$, for $s > s_0^b \approx 0.26$. For the site-centered breather, a pair of multipliers λ, λ^{-1} (with $\lambda > 1$) exists for $s < s_0^s \approx 0.05$, and enters the unit circle for $s > s_0^s$ after a collision at $+1$.

From the above spectral study, one can infer that for harmonic on-site potentials (i.e. $s = 0$) and $\omega = 1.1$, the site-centered breather is weakly unstable and the bond-centered breather is spectrally stable. These results agree with the above results obtained for the DpS equation. This provides a consistent picture, given that the DpS equation correctly approximates breather profiles of amplitudes $\epsilon = O((\omega_b - 1)^2)$ for $\omega_b \approx 1$ (Section 3.2.1). The DpS admits weakly unstable site-centered and stable bond-centered breather solutions, and approximates the dynamics of (9) for $O(\epsilon)$ initial data on times of order $O(\epsilon^{-1/2})$ [26]. Hence, we expect a parallel to the instability of site-centered modes of the DpS dynamics in Eq. (9). Note that these instabilities are extremely small for ω_b close to 1, because the instability of the site-centered breather is already very weak at the renormalized (slow) timescale of the DpS equation (see Fig. 7), and becomes $O(\epsilon^{1/2})$ times weaker at the level of (9) for a breather with amplitude ϵ.

The above picture persists for $s \approx 0$, but the site-centered and bond-centered breathers display a change of stability at the two different critical values $s = s_0^{b,s} > 0$ (s_0^s being quite small), after which their dynamical stability differs from the stability of the DpS breathers. It would be interesting to analyze the possible bifurcations of new types of time-periodic breathers near these critical values of s (perhaps subcritical pitchfork bifurcations at the points $s = s_0^b$, $s = s_0^s$), and this problem will be considered in a future work.

In what follows we illustrate the effect of the additional Floquet eigenvalues close to $+1$ on the breather dynamics, considering the case $\omega_b = 1.1$ and $s = 0$. Fig. 11 compares an eigenvector associated with one of these eigenvalues and the renormalized discrete gradient

$$g_n = \frac{y_{n+1}(0) - y_{n-1}(0)}{\sum_n |y_{n+1}(0) - y_{n-1}(0)|^2},$$

which reveals that the two profiles are very close. The associated mode will thus be referred to as a translation mode or pinning mode, and the effect of a perturbation along its direction is to shift the breather center [43]. This is precisely the type of mode associated with the instabilities reported in Figs. 9 and 10 for $s \in [-1, 1]$.

The existence of this mode has the effect of enhancing the breather mobility. To illustrate this, we perturb at $t = 0$ the velocity components of a stationary breather, adding the discrete gradient g_n multiplied by a velocity factor c. The kinetic energy imprinted to the lattice is then $c^2/2$. We consider below the energy density at the n-th site, which is defined from (6):

$$e_n = \frac{1}{2}\dot{y}_n^2 + W(y_n) + \frac{2}{5}(y_n - y_{n+1})_+^{5/2}. \tag{23}$$

Fig. 12 shows the energy density plot in the system of Eqs. (6)–(8), for a bond-centered breather (with frequency $\omega_b = 1.1$) perturbed with $c = 2 \cdot 10^{-4}$. This perturbation results in a translational motion of the breather at an almost constant velocity with negligible dispersion. A nearly identical figure is obtained for the site-centered breather having the same frequency (result not shown). These results illustrate the strong mobility of discrete breathers in the present model. They are consistent with the approximation E_{PN} of the Peierls–Nabarro barrier computed previously, since we found $E_{PN} \approx 1.77 \cdot 10^{-11}$ for $s = 0$ and $\omega_b = 1.1$ (see Fig. 5). The above momentum perturbation increases the kinetic energy of the bond-centered breather by $c^2/2 = 2 \cdot 10^{-8}$, which is well-above E_{PN}.

To describe the effect of breather perturbations below the Peierls–Nabarro barrier, it is convenient to consider the breather

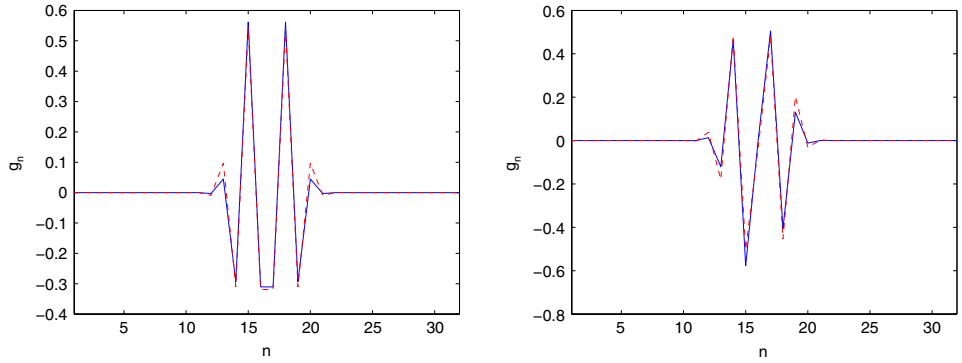

Fig. 11. Pinning mode (full line) and discrete gradient (dashed line) corresponding to a bond-centered (left plot) and site-centered (right plot) stationary breather in system (9), for the breather frequency $\omega_b = 1.1$. The components of the pinning mode correspond to particle positions at $t = 0$ (initial particle velocities vanish).

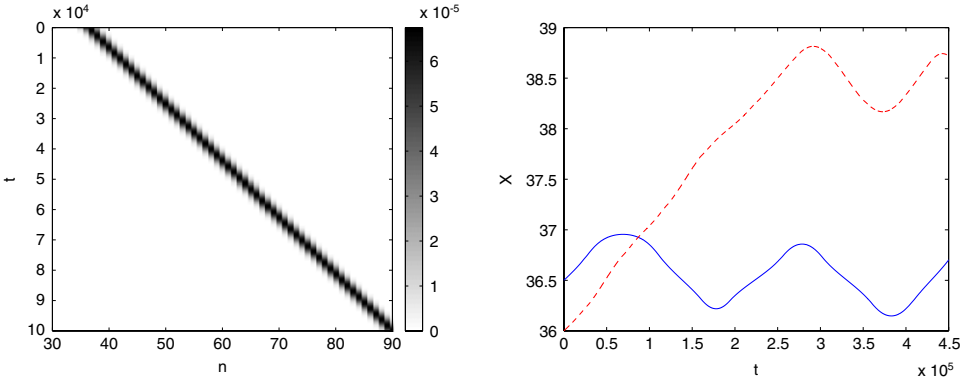

Fig. 12. Left plot: energy density plot of a moving breather in system (6)–(8), obtained by perturbing along the pinning mode a bond-centered stationary breather with frequency $\omega_b = 1.1$. The initial velocity perturbation has a magnitude $c = 2 \cdot 10^{-4}$, and the traveling breather propagates at velocity $v \approx 5.364 \cdot 10^{-4}$. The same type of perturbation applied to a site-centered breather results in a nearly identical figure with $v \approx 5.446 \cdot 10^{-4}$ (result not shown). Right plot: time-evolution of the breather energy center of a bond-centered (full line) and site-centered (dashed line) breather, for a different velocity perturbation $c = 3 \cdot 10^{-6}$, which corresponds to an increase of kinetic energy below the Peierls–Nabarro barrier.

energy center

$$X = \frac{\sum_{n=n'-m}^{n'+m} n e_n}{\sum_{n=n'-m}^{n'+m} e_n} \tag{24}$$

with n' being the location of the maximum energy density of the breather and $m > 0$ an integer which accounts for the width of the breather (we have fixed $m = 5$). Fig. 12 displays $X(t)$ for $c = 3 \cdot 10^{-6}$, i.e. $c^2/2 = 4.5 \cdot 10^{-12}$ lying below E_{PN}. In that case, only the unstable site-centered breather is able to move along the lattice (it is able to jump 2 sites but gets pinned subsequently). For the stable bond-centered breather, a transition from pinning to mobility is obtained for $c > c_c \approx 6.19 \cdot 10^{-6}$. The value of the Peierls–Nabarro barrier resulting from dynamical simulations is thus $c_c^2/2 \approx 1.92 \cdot 10^{-11}$, which is quite close to the approximation E_{PN} computed previously.

The same features can be observed for anharmonic on-site potentials, depending on the stability or instability of the site- or bond-centered breather. More precisely, for $s > s_0^b$, arbitrarily small perturbations along the pinning mode put the unstable bond-centered breather into motion, whereas there is a perturbation threshold for bond-centered breather mobility when $s < s_0^b$. Similarly, for $s < s_0^s$, arbitrarily small perturbations along the pinning mode give rise to site-centered breather motion, and a perturbation threshold for site-centered breather mobility is found when $s > s_0^s$. In addition, in the absence of a mobility threshold, the escape time of the moving breather diverges when the size of perturbation goes to 0.

3.3. Waves resulting from a localized perturbation

3.3.1. Traveling breathers, boomerons and surface modes

Having demonstrated the mobility of breather modes in the DpS equation, in direct analogy with the dynamics of the full oscillator model, we attempt the excitation of the first site of a Newton's cradle and the associated DpS chain, and observe the ensuing space–time evolution.

Consider the Eq. (12) on a semi-infinite lattice with $n \geq 1$ and a free end boundary condition at $n = 1$. We numerically compute the solution of (12) with the initial condition

$$A_1(0) = -i, \qquad A_n(0) = 0 \quad \text{for } n \geq 2. \tag{25}$$

It can be clearly seen in Fig. 13 that the result is the formation of a localized excitation which is traveling robustly through the chain. This is the traveling breather resulting from the mobility of the discrete breathers that we considered before. In addition to this strongly localized excitation, a small amplitude dispersive wave train having a rather complex structure is emitted from the boundary. Until relatively large values of τ, the modulus of the solution displays small variations within an extended region which is broadening with time (shaded area in the left panel of Fig. 13) and decays rather sharply when n is further increased (see the solution profile in the right panel of Fig. 13). We cannot consider this excitation to be a surface mode of the chain [27], as its profile is fairly extended and decays slowly with time. It is rather reminiscent of a self-similar spreading modulated periodic pattern, as shown by the space–time diagram of Fig. 14. At the sharp edge of this regular pattern, high frequency spatial oscillations are generated in a region which is initially small but become thicker as time

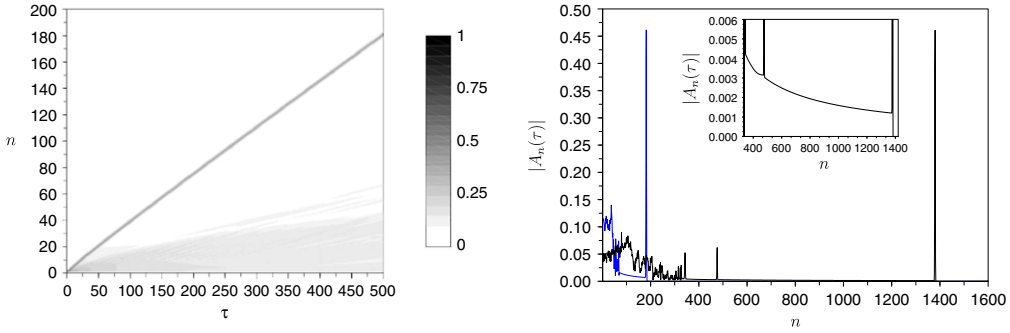

Fig. 13. Evolution of $|A_n(\tau)|$ under the DpS Eq. (12), for the initial condition $A_n(0) = -i\,\delta_{n,1}$ ($\delta_{i,j}$ denotes the usual Kronecker symbol). The space–time diagram (left panel) displays the solution in gray levels. Notice the robust propagating localized mode (traveling breather), as well as the presence of a weak residual (fairly extended) excitation near the boundary. The spatial profile of the solution is shown at two different times (right panel), the blue curve corresponding to $\tau = 502.5$ and the black one to $\tau = 4000$. In the latter case, one can notice the broadening and decay of a dispersive wave train, and the emission of two additional small amplitude traveling breathers, following the main robust localized excitation. The inset provides a zoom on a small amplitude extended wave following the main localized excitation, for $\tau = 4000$. (For interpretation of the references to colour in this figure legend, the reader is referred to the web version of this article.)

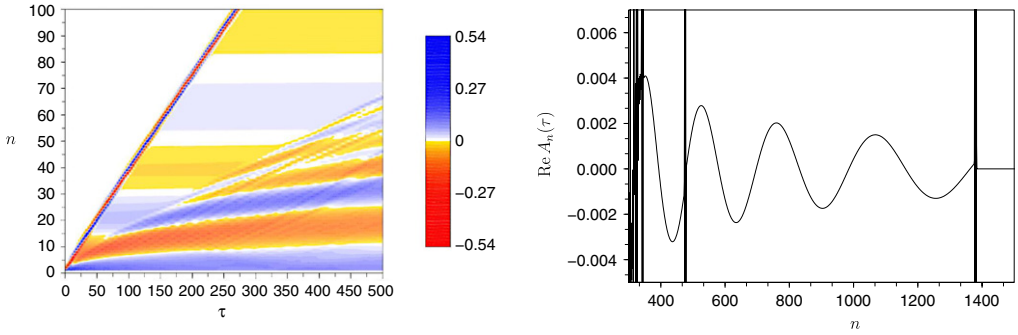

Fig. 14. Real part of the solution $A_n(\tau)$ computed in Fig. 13. The space–time diagram (left panel) shows the propagating localized excitation followed by different modulated spatially periodic patterns. The right panel displays (for $\tau = 4000$) the details of the small amplitude oscillations behind the large amplitude traveling breather.

increases. This behavior is reminiscent of dispersive shocks studied in the FPU model and other nonlinear dispersive Hamiltonian systems (see [44,45] and references therein). Additional small amplitude traveling breathers eventually escape from the dispersive wave train, as shown in the right panel of Fig. 13. In addition, between the large amplitude traveling breather and the highly oscillatory region one observes a slowly modulated periodic pattern of very small amplitude. Its structure is detailed in the right panels of Figs. 13 (inset) and 14. This pattern appears nearly stationary on the timescale of the simulation, as shown in Fig. 14 (left plot).

According to the above numerical observations, the initial perturbation generates a rather complex dynamics which has yet to be explained. The modulated periodic wave following the traveling breather and the macroscopic evolution of the highly oscillatory region might be described in the framework of Whitham's equation [45], using periodic traveling wave solutions of the DpS equation explicitly computed in [21].

For all $\epsilon > 0$ small enough, the above solution of DpS corresponds to an approximate solution of (9) given by (13), satisfying $y_n^{\text{app}}(0) = 0$, $\dot{y}_1^{\text{app}}(0) = 2\epsilon + O(\epsilon^{3/2})$, $\dot{y}_2^{\text{app}}(0) = O(\epsilon^{3/2})$ and $\dot{y}_n^{\text{app}}(0) = 0$ for $n \geq 3$. Fig. 15 compares this approximate solution and the solution of (9) with initial condition

$$y_n(0) = 0, \qquad \dot{y}_1(0) = 2\epsilon, \qquad \dot{y}_n(0) = 0 \quad \text{for } n \geq 2 \tag{26}$$

for a small value of ϵ. One can see that the DpS equation and the full oscillator model give rise to similar dynamics, i.e. the initial impulse splits into a traveling breather followed by a small oscillatory tail and a dispersive wave train. Note that the profiles of the exact and approximate solutions are quite close over a long transient, but the traveling breather velocity is slightly overestimated by the DpS approximation (13). Fig. 16 (left panel) describes the energy density in Newton's cradle after the initial perturbation (26). The propagation of a localized excitation at an almost constant velocity is clearly visible, as well as the broadening and decay of the dispersive wave train emitted from the boundary. The modulated periodic patterns previously obtained with the DpS equation correspond (via the ansatz (13)) to modulated periodic traveling waves propagating in Newton's cradle. Their structure is detailed in Fig. 16 (right panel). The different strips correspond (from top to bottom) to the traveling breather excitation followed by a small oscillatory tail, and the dispersive wave train including a highly oscillatory region followed by slowly modulated periodic traveling waves. As we previously conjectured, different parts of the wave train might be described (via Whitham's equation) as modulations of the periodic traveling waves analyzed in [21].

The DpS approximation becomes inaccurate when the initial velocity is not small, but the phenomena described above are still observed provided the initial velocity is not too large or for sufficiently long chains. In addition, the dynamics at high initial velocity displays new dynamical features illustrated by Figs. 17 and 18 (for $\dot{y}_1(0) = 10^6$ and a chain of 1400 particles). At the early stage of the dynamics (i.e. over a few periods of local oscillations), a wave train is emitted from the boundary, with two soliton-like excitations appearing at its edge (Fig. 17). This is reminiscent of the phenomenology described in [7,5]. As the localized waves propagate from one site to the next, their amplitudes get slowly modulated (for the above initial velocity, the period of internal oscillations is around 170 times larger than the inverse wave velocity). The two pulsating solitary waves correspond in fact to a traveling breather whose internal oscillations are very slow compared to its velocity. Fig. 18 illustrates the traveling breather profile, displaying two different nearly-symmetric configurations at different times. One can notice important differences with the case of small initial velocities detailed in Fig. 15. In the present

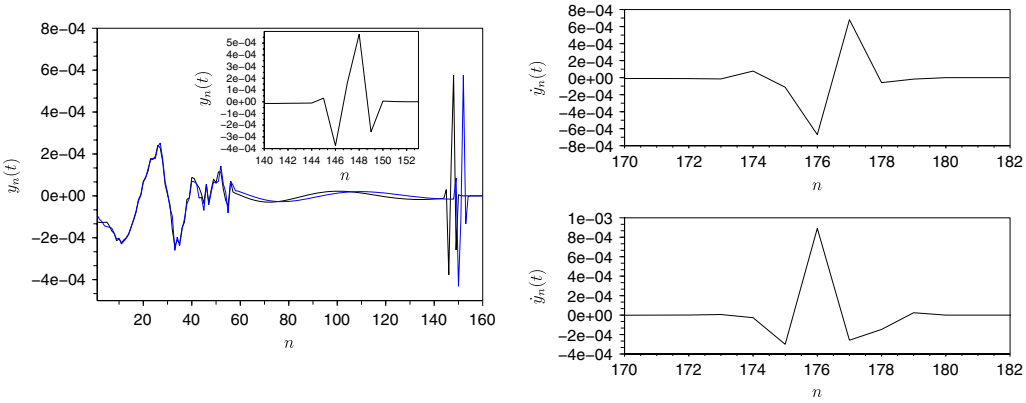

Fig. 15. Left: comparison between the solution of (9)–(26) (black curve) and its approximation given by (12)–(13)–(25) (blue curve), for a small amplitude initial excitation with $\epsilon = 0.9548 \cdot 10^{-3}$. Particle displacements $y_n(t)$ are plotted at a fixed time $t = 13432$ (corresponding to $\tau \approx 415$). The inset displays a zoom on the traveling breather excitation propagating in the nonlinear chain (9). Right: particle velocities in system (9) near the traveling breather excitation, at two different times $t = 16173.5$ (top) and $t = 16177.5$ (bottom) where the profiles have two different odd- and even-parity symmetries. (For interpretation of the references to colour in this figure legend, the reader is referred to the web version of this article.)

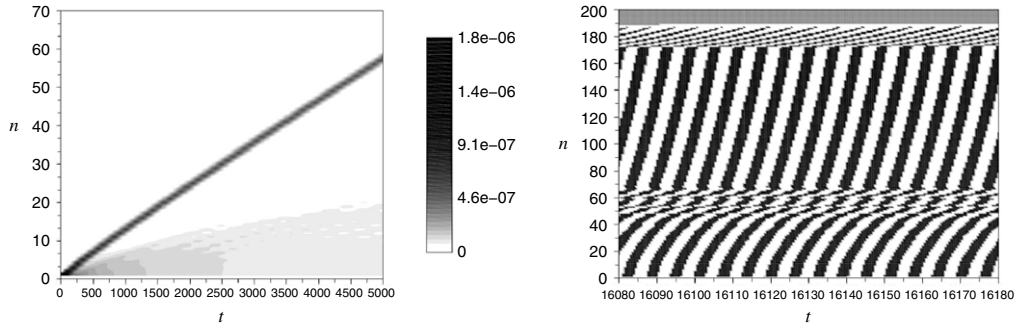

Fig. 16. Left : energy density (23) in system (9) after the initial perturbation (26) with $\epsilon = 0.9548 \cdot 10^{-3}$, plotted for $t \in [0, 5000]$. Right : sign of the particle displacements $y_n(t)$ in a shorter time interval, for $t \in [16080, 16180]$. White corresponds to positive values, black to negative values and gray to vanishing displacements.

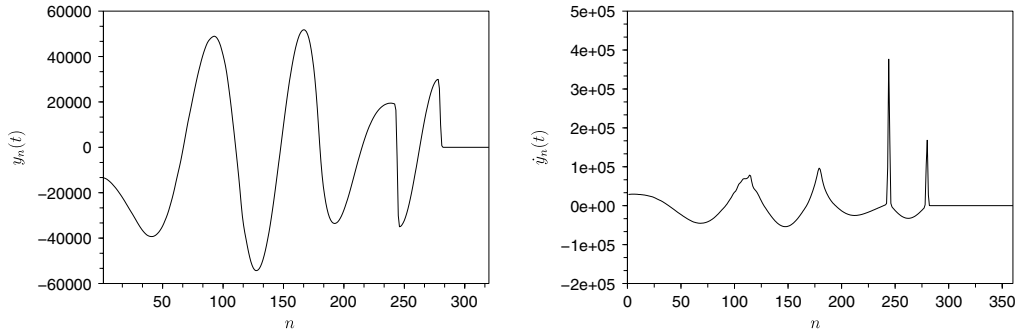

Fig. 17. Solution of (9)–(26) for the initial velocity $\dot{y}_1(0) = 10^6$. The spatial profiles of particle displacements (left panel) and velocities (right panel) are plotted at $t = 23.63$. Two localized compression waves reminiscent of Nesterenko's soliton are visible near the sites $n = 280$ and $n = 244$.

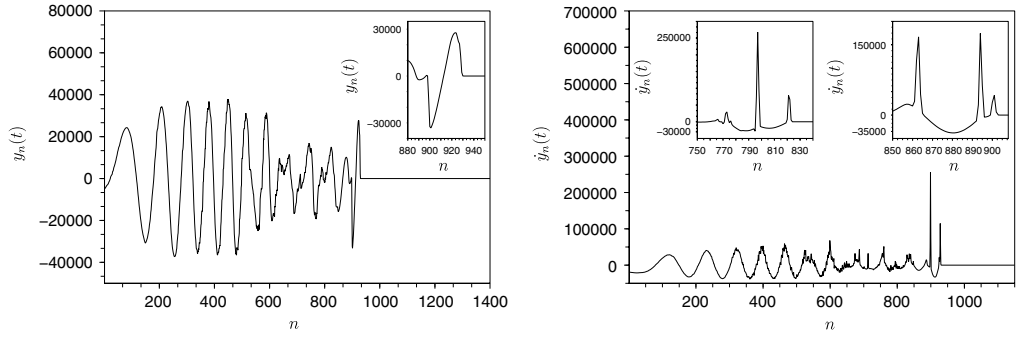

Fig. 18. Same as in Fig. 17, with the solution plotted at a later time $t = 96.58$. The inset in the left panel details particle positions near the traveling breather excitation at $t = 96.58$. The right panel insets provide a zoom on particle velocities at $t = 83.75$ (left) and $t = 93.15$ (right), showing the transition between two different configurations displaying some imperfect reflectional symmetry.

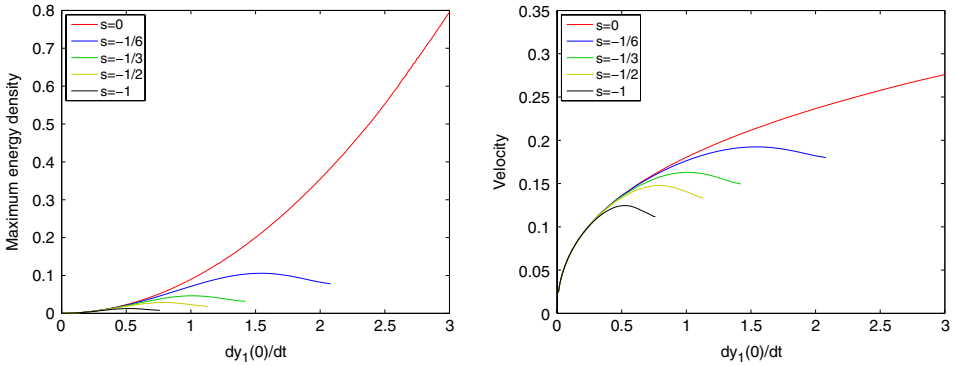

Fig. 19. Maximum energy density (left plot) and velocity (right plot) of the traveling breather generated in system (6)–(10) with initial condition (26), for several values of $\dot{y}_1(0)$ and anharmonicity parameter $s \leq 0$.

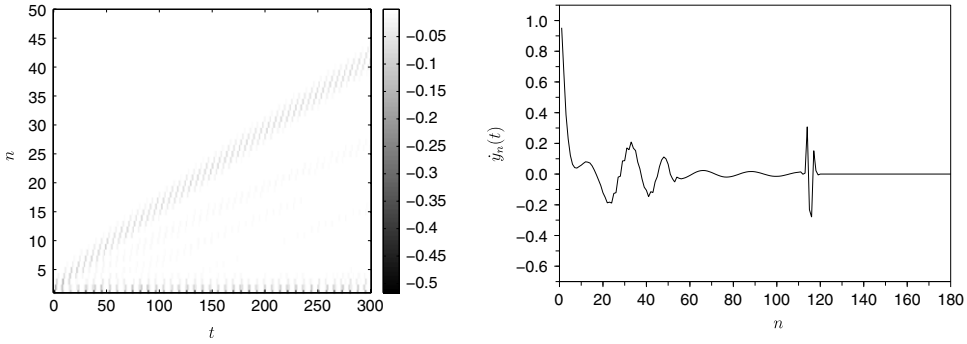

Fig. 20. This figure illustrates the excitation of a surface mode and a traveling breather in system (6)–(10) with $s < 0$, following a perturbation of the first particle (initial condition (26)). Left plot: space–time diagram showing the interaction forces $f_n = -(y_n - y_{n+1})_+^{3/2}$ for $s = -0.7$ and $\dot{y}_1(0) = 0.94$. Forces are represented in gray levels, white corresponding to vanishing interactions (i.e. beads not in contact) and black to a minimal negative value of the contact force. Right plot: snapshot of particle velocities at $t \approx 587$, for $s = -1/6$ and $\dot{y}_1(0) \approx 1.87$.

case, the breather has a much broader spatial extent and displays a different velocity profile. In addition, the localized excitation is followed by a larger (and more irregular) oscillatory tail, in which steepenings of wave crests give birth to new soliton-like excitations and dispersive shocks.

In what follows we analyze the effect of considering the local anharmonic potential (10). Due to the smoothness of W, the DpS equation remains unchanged with respect to the harmonic case, as observed in Section 3.1.2. Consequently, the dynamics of (9) after the impact is expected to remain unchanged for small excitations, on the time scales given in Section 3.1.2. However, it is interesting to examine possible additional effects of anharmonicity occurring on longer time scales or for large amplitude excitations. For example, a trapping of large amplitude traveling breathers can occur in Klein–Gordon lattices [34,35], due to the Peierls–Nabarro energy barrier separating site-centered and bond-centered breathers.

In order to characterize the breather motion we consider the traveling breather energy center $X(t)$ defined by (24). The average velocity of the traveling breather is computed as the slope of the linear least squares approximation of the function $X(t)$, taking only into account the points for which the traveling breather is sufficiently far from the boundary in order to eliminate boundary effects. Fig. 19 displays the traveling breather velocity and maximum energy density (computed from (23)) as a function of the initial velocity $\dot{y}_1(0)$, for different values of the parameter $s \leq 0$. As expected, the different graphs are very close at small initial velocity where the DpS equation drives the dynamics. In this regime, the traveling breather velocity scales as the square root of the initial velocity, as it follows from the ansatz (13).

Discrepancies with the DpS approximation appear at larger velocities depending on the magnitude of s. In particular, for $s < 0$ the graphs of Fig. 19 are interrupted above some critical velocities, because the solution blows-up in finite time when the initial velocity exceeds some threshold. Below this value, the anharmonicity of the on-site potential with $s < 0$ decreases the breather velocity. The energy of the traveling breather (including its kinetic energy) becomes much smaller because a part of the initial energy remains trapped in the form of a surface mode located near $n = 1$. The possibility of exciting a surface mode by an impact was already pointed out in reference [46], for a mixed Klein–Gordon-FPU chain with a sinusoidal local potential, and a Morse interaction potential instead of the fully-nonlinear Hertzian interactions. This phenomenon is illustrated in Fig. 20 for $s = -0.7$, where the initial perturbation $\dot{y}_1(0) = 0.94$ generates a surface mode and a traveling breather of smaller amplitude. In a companion paper [37], we have numerically computed these surface modes using the Newton method. For $s < 0$, we have found spectrally stable surface modes with frequencies $\omega_s \approx 1$ lying below unity (although linear instabilities occur at low enough frequencies). When $\omega_s \to 1$, their energy and amplitude vanish, opening the possibility of exciting such modes for arbitrarily small initial velocities of the first particle.

Note that the above-mentioned blow-up phenomenon is due to potential (10) with $s < 0$ and does not occur for $W(y) = 1 - \cos y$, which corresponds e.g. to the gravitational potential acting on the usual Newton's cradle. In the latter case, the dynamics resulting from the impact becomes rather similar to the phenomena studied in [46]. For sufficiently large impact velocities the traveling breather is replaced by a kink reminiscent of Nesterenko's soliton [5], resulting in the ejection of a finite number of particles at the end of the chain (result not shown).

In the case $s > 0$ of (10) we can observe a different scenario, illustrated by Fig. 21 for $s = 1$. The traveling breather does not move at constant velocity, but instead behaves like a "bouncing

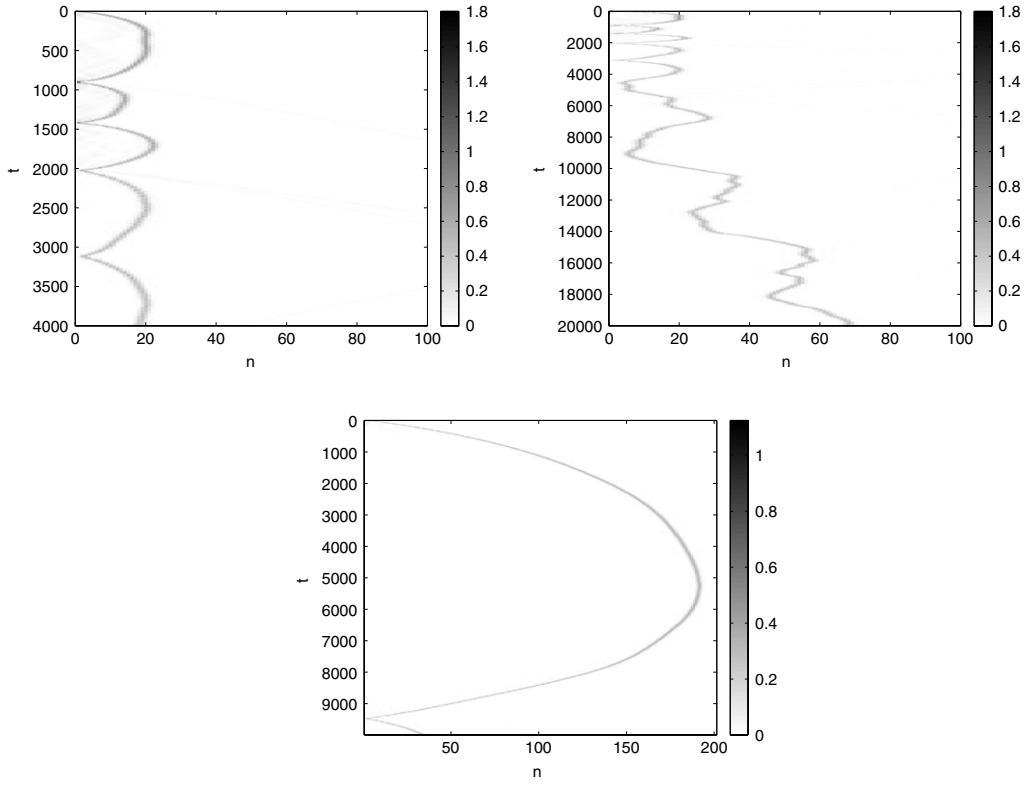

Fig. 21. Illustration of the direction-reversing phenomenon occurring during traveling breather propagation, for the on-site potential (10) with $s = 1$ and an initial condition of the form (26). The space–time diagrams indicate the energy density (23). The upper left plot corresponds to $\dot{y}_1(0) = 1.9$. During a few rebounds, the breather center behaves like a Newtonian particle in an almost constant effective force field, alternating phases of deceleration, direction-reversing, accelerated backward motion and rebound at the boundary. The upper right plot corresponds to larger integration times, on which an erratic breather motion and phases of intermittent trapping can be observed. The bottom plot corresponds a lower initial velocity $\dot{y}_1(0) = 1.5$, for which the traveling breather deceleration becomes much smaller.

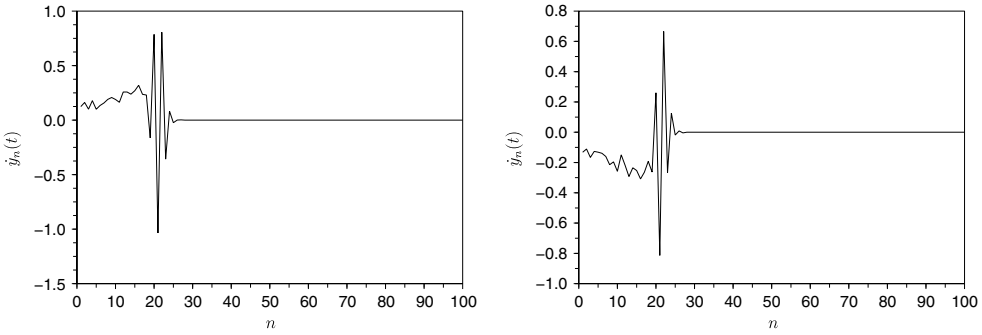

Fig. 22. Particle velocities for $s = 1$ and the initial condition (26) with $\dot{y}_1(0) \approx 1.87$. The traveling breather profile is shown at two different times close to direction-reversing (the left panel corresponds to $t \approx 238$, and the right panel to $t \approx 241$). Nonlinear waves confined between the traveling breather and the boundary are also visible.

ball" against the boundary at $n = 1$, i.e. it experiences alternating phases of deceleration, direction-reversing, accelerated backward motion towards the boundary, and rebound at the boundary (top left panel of Fig. 21). During a few rebounds, the breather center behaves like a Newtonian particle in an almost constant effective force field, which increases with the imprinted initial velocity (compare the top and bottom panels) and with the anharmonicity parameter s (results not shown). Fig. 22 displays a traveling breather profile at the onset of direction-reversing. The rebound dynamics can be followed by phases of intermittent trapping or erratic motion of the breather (Fig. 21, top right panel).

These traveling breathers with direction-reversing motion are reminiscent of excitations known as "boomerons", consisting of direction-reversing solitons discovered in different kinds of integrable models (see [28] and references therein), but the link between both phenomena remains quite speculative at this stage. Although we have no clear explanation of the origin of direction-reversing for the traveling breather, one possibility might be its interaction with other nonlinear waves visible in Fig. 22, which are confined between the traveling breather and the boundary.

To complete the results of Fig. 21, it is interesting to notice that the traveling breather can reach the opposite side of a finite chain before direction-reversal when s is fixed and $\dot{y}_1(0) = 2\epsilon$ is sufficiently small. Indeed, the solution of system (6)–(10) remains close to the DpS approximation for bounded values of $\tau = \epsilon^{1/2}t$ (i.e. over long times $t = O(\epsilon^{-1/2})$) when ϵ is small enough in (26) [26]. According to our numerical observations, the traveling breather solution of the DpS system (12)–(25) propagates monotonically through the chain. Consequently, the traveling breather solution of (6)–(10) does not display any spontaneous

direction-reversal while traveling through the chain, provided $\dot{y}_1(0)$ is small enough. The same phenomenon can occur in a finite chain when $\dot{y}_1(0)$ is fixed and $s > 0$ is small enough, since spontaneous direction-reversal is not observed for $s = 0$, and the trajectories of (6)–(10)–(26) depend continuously on $s \in [0, +\infty)$ in the uniform topology on bounded time intervals. However, on the basis of numerical simulations realized for different values of s and initial velocities, we conjecture that direction-reversal may take place in semi-infinite chains as soon as $s > 0$ and $\dot{y}_1(0) \neq 0$ in (26). According to the above arguments, we expect the first direction-reversal to occur at some time $t = T(\epsilon, s)$ satisfying $\lim_{\epsilon\to 0}\left(\epsilon^{1/2} T(\epsilon, s)\right) = +\infty$ and $\lim_{s\to 0^+} T(\epsilon, s) = +\infty$.

Lastly, we would like to comment on the absence of surface mode excitation observed in Fig. 21 for $s = 1$. In the work [37], we have computed surface mode solutions of the chain for $s = 1$ using the Newton method. We have obtained spectrally stable surface modes with frequencies lying above (and close to) $\omega_{\min} \approx 1.96$, whose energies lie above some finite threshold. Such modes cannot be excited with the initial perturbations considered in Fig. 21, whose energies lie well below this excitation threshold.

3.3.2. Traveling breathers resulting from impacts in stiff Newton's cradles

As seen in the previous section, a small velocity perturbation at the end of a Newton's cradle results in the propagation of a highly localized traveling breather at an almost constant velocity, well separated from a much slower dispersive wave train. This dynamics is driven by the DpS equation governing the nonlinear evolution of small initial data over long (but finite) times. When the initial velocity is not small, we have identified in Newton's cradle different types of dynamical phenomena which are not described by the DpS equation. These phenomena depend on the on-site potential : observation of soliton-like localized waves at high initial velocities for harmonic potentials, excitation of a surface mode of significant amplitude for soft potentials, and generation of a direction-reversing traveling breather for hard potentials.

In this section, we analyze conditions under which mechanical systems involving Hertzian interactions and local potentials do not exhibit the above phenomena, so that the main pressure wave propagates almost freely in the form of a highly localized traveling breather. For this purpose, we have to discuss under which physical conditions the DpS equation drives the dynamics. This analysis is done in Section 3.3.2.1, where we derive a dimensionless parameter λ characterizing the DpS regime. From this study, we recover the fact that the usual Newton's cradle acting under gravity lies far beyond the DpS regime (it supports soliton-like excitations instead of traveling breathers [7,5]). However, the analysis of Section 3.3.2.1 can be used as a guide to define other mechanical models supporting traveling breather excitations. In Section 3.3.2.2, we introduce such a system consisting of a chain of stiff cantilevers decorated by spherical beads, calibrated using realistic material parameter values.

Traveling breathers described by the DpS equation could have interesting applications for the control of stress waves in granular systems, since they allow for a coherent and highly-localized energy transport. Moreover, the internal oscillation of traveling breathers may allow resonance phenomena to occur, opening e.g. the possibility of breather interactions with defect modes of the chain. As an application, we show in Section 3.3.2.2 that the above cantilever chain can act effectively as a granular shock reflector.

3.3.2.1. Dimensional analysis of the DpS limit. In Sections 3.1.2 and 3.3.1, we have described the DpS limit and the associated dynamical regime for Eq. (9) written in a normalized form (or for its generalization with local anharmonicity (10)). In this section, we consider a chain of identical beads of mass m sitting in local anharmonic potentials, described by the Hamiltonian

$$\mathcal{H} = \sum_n \frac{m}{2}\dot{x}_n^2 + \frac{k}{2}x_n^2 + \frac{\tilde{s}}{4}x_n^4 + \frac{2}{5}\gamma(x_n - x_{n+1})_+^{5/2}, \tag{27}$$

where γ is the nonlinear stiffness of Hertzian interactions, k the linear stiffness of local potentials and $\tilde{s}$ measures the strength of local anharmonicity. Our aim is to analyze the evolution of the initial condition

$$x_n(0) = 0, \qquad \dot{x}_n(0) = V\,\delta_{n,1}. \tag{28}$$

In what follows, we use suitable scalings to rewrite this problem in normalized form. This allows us to analyze in which parameter regime the DpS equation drives the dynamics, which induces the propagation of a traveling breather as described in Section 3.3.1. As we shall see, this case occurs when the initial velocity is sufficiently small compared to a reference value depending on parameters.

Let us first consider two interacting beads, one being initially at rest and the other having an initial velocity V, and temporarily neglect the local restoring force of the on-site potentials. After collision, their contact time is approximately equal to $2.43\,\tau_h$ with $\tau_h = [m^2/(\gamma^2 V)]^{1/5}$, and their maximal compression distance is close to $0.76\,\delta$, where $\delta = (mV^2/\gamma)^{2/5}$ [47,6]. Moreover, the stiffness constant of Hertzian interactions linearized at precompression δ is of the order of $\kappa_h = \gamma\sqrt{\delta}$.

Including back the local restoring forces, the displacement ξ at which Hertzian and local forces equilibrate satisfies $\gamma\,\xi^{3/2} = k\,\xi$ and is given by $\xi = (k/\gamma)^2$. In addition, the period of local oscillations is $2\pi\,\tau_c$ with $\tau_c = (m/k)^{1/2}$.

Now we are ready to perform a suitable rescaling of (27). Setting $x_n(t) = \xi\,y_n(t/\tau_c)$, the Hamiltonian (27) is mapped to the normalized form (6)–(10) with $s = \tilde{s}\xi^2/k$. Moreover, the initial condition (28) reads in dimensionless form

$$y_n(0) = 0, \qquad \dot{y}_n(0) = \lambda^{5/2}\,\delta_{n,1}, \tag{29}$$

where

$$\lambda = \frac{\kappa_h}{k} \tag{30}$$

measures the relative strengths of the Hertzian interaction at initial velocity V and the local potential. Since $\kappa_h = m/\tau_h^2$, we have equivalently

$$\lambda = \frac{m}{k\tau_h^2}, \tag{31}$$

i.e. $\lambda^{1/2}$ measures (up to a multiplicative constant) the relative duration of local oscillations and binary collisions of free beads.

From (29) and the results of Section 3.3.1, we deduce that the DpS regime giving rise to (almost) freely-propagating breathers takes place when $\lambda^{5/2}$ is small enough. According to definition (30), the linear stiffness of local oscillators must dominate the effective Hertzian stiffness κ_h, which depends on the initial velocity. Equivalently (from Eq. (31)), local linearized oscillations must be sufficiently fast compared to the collision of two free beads occurring at the given initial velocity. In addition, one can observe that $\lambda^{5/2} = V/V_c$ with $V_c = m^{-1/2}\,k^{5/2}\,\gamma^{-2}$. Consequently, the DpS equation drives the dynamics when the initial velocity is small compared to the reference velocity V_c determined by the model parameters.

To illustrate the above computations, let us consider the excitation of the first bead of a classical Newton's cradle (as represented in Fig. 1), in which the local potential is due to gravity. In this system, impact propagation is usually analyzed under the assumption of small bead displacements [23], leading to the case $\tilde{s} = 0$ of (27). The period of local oscillations (generally of the order of a second) being much larger than the collision time between two

beads (typically of the order of 0.1 ms [47]), we are then extremely far from the DpS regime. For example, for a classical Newton's cradle with strings of length 50 cm and binary collision time $2.43\,\tau_h = 0.077$ ms (value taken from [47] for an impact velocity of 1.1 m.s^{-1}), one obtains $\lambda^{5/2} \approx 1.75 \cdot 10^{19}$. In that case, the propagating wave takes the form of a soliton-like excitation which is reminiscent of the primary compression pulse represented in Fig. 17.

In Section 3.3.2.2, we introduce a mechanical system for which local oscillators are much stiffer and the DpS dynamics becomes relevant.

3.3.2.2. Application to a chain of cantilevers decorated by spherical beads. Several types of mechanical models have been devised to analyze the properties of discrete breathers experimentally, see e.g. [48–51]. In this section we introduce a simplified model of the cantilever system sketched in Fig. 1 (right picture). We consider the form (27) analyzed previously (restricting ourselves to harmonic on-site potentials) and examine the more general situation when the lattice is spatially inhomogeneous. With this model, we shall observe that a moving breather generated by an impact on the first cantilever can be almost totally reflected by a localized impurity corresponding to a moderate increase of the bead radii on a single cantilever.

We begin by introducing a simplified model of the cantilever system of (the right panel of) Fig. 1, where cantilever compression is neglected and bead deformations are treated quasi-statically. More precisely, each bead is seen as an elastic medium at equilibrium, clamped at a cantilever at one side, and either free or in contact with one bead of a neighboring cantilever at the opposite side. So any bead deformation is fully determined by two cantilever positions, and can be approximated by Hertz's contact law. In addition, each cantilever decorated by two spherical beads is described by a point-mass model which approximates the dynamics of the slower bending mode, following a classical approach in the context of atomic force microscope cantilevers [52]. Under these approximations, our model incorporates a single degree of freedom per cantilever, namely its maximal deflection.

The point-mass model is obtained as follows. Using a rod model and under the assumption of small deflection, a cantilever clamped at both ends and bent by a force applied to its mid-point can be represented by an equivalent linear spring of stiffness $k = 192\,E\,I\,\ell^{-3}$, where E is the cantilever's Young modulus, ℓ its length and $I = w\,h^3/12$ its area moment of inertia, w, h denoting the cantilever width and thickness respectively (see e.g. [53, pp. 77 and 81]). For a cantilever without attached beads, the first bending mode frequency satisfies $\omega_{\min} \approx 22.4\,[EI/(\rho A)]^{1/2}\ell^{-2}$ ([53], p.102) where ρ denotes the cantilever density and $A = w\,h$ its cross section. A single cantilever is then represented by an effective mass $m^* = k/\omega_{\min}^2 \approx 0.38\,m_c$, where $m_c = \rho A \ell$ is the exact cantilever mass. The effective mass of a cantilever decorated by two beads of masses m_b is then $m = m^* + 2m_b$. For beads of radius R and density d we fix consequently $m = 0.38\,m_c + (8/3)\pi\,dR^3$.

Now let us describe the model for a one-dimensional chain of such cantilevers, where all beads are made of the same material with Young's modulus $\mathcal{E}$ and Poisson coefficient ν. We denote by $R_n = R\,\tilde{R}_n$ the radius of the two beads of the nth cantilever (R being a reference value and $\tilde{R}_n$ an adimensional number), $x_n(t)$ the maximal cantilever deflections and $m_n = 0.38\,m_c + (8/3)\pi\,dR_n^3$ their effective masses. The array of decorated cantilevers is then described by the Hamiltonian

$$\mathcal{H} = \sum_n \frac{m_n}{2}\,\dot{x}_n^2 + \frac{k}{2}\,x_n^2 + \frac{2}{5}\,\gamma_n (x_n - x_{n+1})_+^{5/2}, \tag{32}$$

where $\gamma_n = \gamma\,\eta_n$ is the nonlinear stiffness constant of Hertzian interactions between two beads on different cantilevers n and $n+1$, defined by $\gamma = \frac{\mathcal{E}\sqrt{2R}}{3(1-\nu^2)}$ and $\eta_n = [2\tilde{R}_n\tilde{R}_{n+1}/(\tilde{R}_n + \tilde{R}_{n+1})]^{1/2}$ (see e.g. [53]). Note that m_n and γ_n are constant in the particular case when R_n is constant, which leads to the homogeneous system (27) (or its normalized form (6)) previously analyzed.

Setting $x_n(t) = \xi\,y_n(t/\tau_c)$ as in Section 3.3.2.1, the Hamiltonian (32) yields the following equations of motion in dimensionless form

$$\mu_n \ddot{y}_n + y_n = \eta_{n-1}(y_{n-1} - y_n)_+^{3/2} - \eta_n (y_n - y_{n+1})_+^{3/2}, \tag{33}$$

where $\mu_n = m_n/m$. In particular, if all beads have radius R (i.e. $\tilde{R}_n = 1$) then $\eta_n = \mu_n = 1$ and one recovers system (9).

Our main purpose is to analyze an impact problem in a chain of N cantilevers with free end boundary conditions, where the first cantilever is hit by a striker at $t = 0$. For this purpose we consider a simpler initial condition where all cantilevers with index $n \geq 2$ are initially at rest and the first cantilever has initial velocity V and zero deflection. This corresponds to fixing the initial condition (28), which yields (29) in rescaled form.

Numerical simulations are performed for a chain of $N = 200$ stainless steel cantilevers with $\rho = 8 \cdot 10^3$ kg.m^{-3}, $E = 193$ GPa, $\ell = 25$ mm, $w = 5$ mm, $h = 1$ mm, decorated by teflon beads with $d = 2.2 \cdot 10^3$ kg.m^{-3}, $\mathcal{E} = 1.46$ GPa, $\nu = 0.46$ [9]. All beads have radius $R = 2.38$ mm, except at the middle of the chain where $\tilde{R}_{100}$ can be tuned.

We fix the impact velocity $V = 1$ m.s^{-1}, which yields $\tau_h \approx 0.047$ ms. Since $\tau_c \approx 0.025$ ms, we have $\lambda \approx 0.29$ and $\lambda^{5/2}$ is small. Consequently, according to the results of Section 3.3.2.1, the DpS approximation is valid in the spatially homogeneous case, or in sufficiently long homogeneous segments of a chain including defects. As a result, the initial impact generates a traveling breather and a fairly extended wave train emitted from the boundary, as previously described in Section 3.3. From our simulations, the traveling breather velocity is close to 2030 sites per second. Evaluating the traveling breather characteristics at $n = 80$, we find a maximal bead velocity close to 0.5 m.s^{-1} (i.e. half the impact velocity), a maximal cantilever deflection close to 11 μm and a maximal interaction force close to 2.8 N. The pulse duration is close to 3.8 ms and the period of internal oscillations close to 0.14 ms $\approx T_0/(1.1)$, $T_0 = 2\pi\,\tau_c$ being the period of linear local oscillations.

When the breather reaches the defect site, it appears to be almost totally reflected for a large enough inhomogeneity, whereas it remains significantly transmitted for a sufficiently small inhomogeneity. This phenomenon is illustrated by Fig. 23, which compares the cases $\tilde{R}_{100} = 1.6$ (almost total reflection) and $\tilde{R}_{100} = 1.1$ (partial reflection), showing the high sensitivity of the reflection to the strength of the inhomogeneity. After the breather reflection by the defect for $\tilde{R}_{100} = 1.6$, a small part of the vibrational energy remains loosely trapped near the defect site (an excitation not visible in Fig. 23 due to smallness of interaction forces). Such phenomena resulting from breather–defect interactions have been already numerically observed in different types of Klein–Gordon lattices (see [54,55] and references therein). In the present model, almost total reflection occurs for physically realistic parameter values, which suggests potential applications of such systems as shock wave reflectors.

To close this section, let us note that the other dynamical regimes identified in Section 3.3 may be also of practical interest. Another shock-redirection mechanism exists for hard anharmonic on-site potentials, which yield direction-reversing traveling breathers for large enough impact velocities (see Fig. 21). This suggests that both reflection mechanisms (based either on defects or hard local anharmonicity) could be combined to devise an efficient shock wave reflector working for a large range of impact velocities. In addition, the surface modes observed for a soft on-site anharmonicity may have potential applications for energy scavenging, or for the design of acoustic diodes [4].

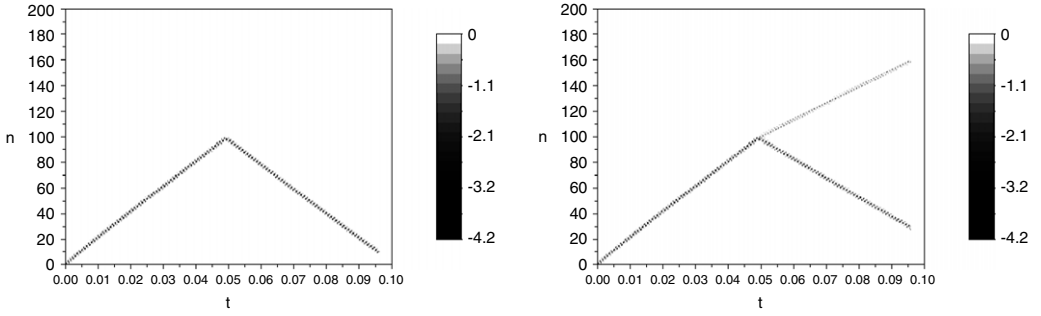

Fig. 23. Space–time diagrams showing the interaction forces $f_n = -\gamma_n(x_n - x_{n+1})_+^{3/2}$ in system (32) for the impact problem described in the text (forces are expressed in N). Forces are represented in gray levels, white corresponding to vanishing interactions (i.e. beads not in contact) and black to a minimal negative value of the contact force. Left plot: $\tilde{R}_{100} = 1.6$. Right plot: $\tilde{R}_{100} = 1.1$.

4. Traveling breathers under precompression

In Section 3 we have analyzed the properties of discrete breathers in chains of oscillators coupled by fully nonlinear Hertzian interactions. We have obtained highly-localized static breathers, which display a super-exponential spatial decay and have an almost constant width in the small amplitude limit. Moreover, small perturbations of the static breathers along a pinning mode generate traveling breathers propagating at an almost constant velocity with very small dispersion.

These properties are largely due to the fully-nonlinear coupling between oscillators, which reduces the phonon band to a single frequency. Intuitively, the absence of linear coupling terms enhances localization, because linear dispersion tends to disperse localized wave packets. Though this phenomenon can be compensated by nonlinearity, breathers in nonlinear lattices with phonon bands generally have a slow exponential spatial decay in the limit of vanishing amplitude (see e.g. [18,38]). Moreover, due to resonance with phonons, exact traveling breathers are generally superposed on non-decaying oscillatory tails, a phenomenon mathematically analyzed in a number of works (see [39,56,57] and references therein). Only under special choices of the speed (or the system parameters) can it then be the case that the amplitude of these oscillatory tails exactly vanishes [58,59].

Due to these noticeably different breather properties in the presence or absence of a phonon band, it is interesting to consider physical systems possessing a tunable phonon band, allowing to pass from one situation to the other. This is the case in particular for granular crystals under tunable precompression, since the latter results in a perturbation of the interaction potential inducing an additional harmonic component.

In this section, we incorporate the precompression effect to model (6), formally analyze the existence of discrete breathers through the phenomenon of modulational instability, and numerically demonstrate that the existence of a phonon band can drastically modify the outcome of an initial impact.

4.1. Granular chain under precompression, and correspondence to the NLS equation

We consider the system (6)–(10) with the modified interaction potential

$$V(r) = \frac{2}{5}(d-r)_+^{5/2} + d^{3/2}r - \frac{2}{5}d^{5/2}, \tag{34}$$

where $d > 0$ is a parameter. We have thus for $r \approx 0$

$$V(r) = v_1\frac{r^2}{2} + v_2\frac{r^3}{3} + v_3\frac{r^4}{4} + O(|r|^5),$$

with $v_1 = \frac{3}{2}d^{1/2}$, $v_2 = -\frac{3}{8}d^{-1/2}$, $v_3 = -\frac{1}{16}d^{-3/2}$. This modified potential possesses a harmonic component of size $d^{1/2}$ in the neighborhood of the origin, and it becomes linear for $r \geq d$. The first term of (34) corresponds to the classical Hertzian potential including a precompression effect. For example, this type of interaction can be achieved in the cantilever system of Fig. 1 by applying a force at both ends when the cantilevers are unclamped, which results in a uniform compression of all the beads by a distance d, and by clamping the cantilevers at this new equilibrium state. The second and third terms of (34) do not modify the equations of motion, and just aim at putting the modified Hertz potential in a standard form with $V(0) = 0, V'(0) = 0$.

System (6)–(10)–(34) consists of a mixed Klein–Gordon – FPU lattice. The dynamical equations linearized at $y_n = 0$ admit solutions consisting of sinusoidal waves (or phonons) $y_n(t) = A\,e^{i\,(qn-\omega t)} + \text{c.c.}$, which obey the dispersion relation

$$\omega^2(q) = 1 + 2v_1(1-\cos q), \tag{35}$$

where $q \in [0, \pi]$ denotes the wavenumber and ω the phonon frequency. Due to precompression, phonon frequencies belong now to a band of finite width (of size $O(d^{1/2})$ when $d \approx 0$).

For this class of systems combining anharmonic local and interaction potentials, the modulational instability (MI) of small amplitude periodic and standing waves has been studied in a number of references (see e.g. [60,29]). This phenomenon can be analyzed through the continuum nonlinear Schrödinger equation, which describes the slow spatio-temporal modulation of small amplitude phonons under the effects of nonlinearity and dispersion. Indeed, from the general results of [30,31], system (6)–(10)–(34) admits solutions of the form

$$y_n(t) = \epsilon A[\epsilon^2 t, \epsilon(n - c\,t)]\, e^{i(qn-\omega t)} + c.c. + O(\epsilon^{3/2}) \tag{36}$$

on time intervals of length $O(\epsilon^{-2})$ (ϵ being a small parameter), where $A(\tau, \xi)$ satisfies the NLS equation

$$i\partial_\tau A = -\frac{1}{2}\omega''(q)\,\partial_\xi^2 A + h|A|^2 A. \tag{37}$$

In the above expressions, ω is given by (35), $c = \omega'(q)$ is the group velocity, $h = \beta/\omega$, $\omega'' = v_1\omega_2/\omega$ and we have (see [30, equation (2.12) p. 557]),

$$\beta = \frac{16v_2^2(\sin q)^2(1-\cos q)^2}{4v_1(1-\cos q)^2 + 3} + \frac{3}{2}[4v_3(1-\cos q)^2 + s],$$

$$\omega_2 = \cos q - \frac{v_1}{\omega^2}(\sin q)^2.$$

The so-called focusing case of the NLS equation [10] occurs for $\omega''(q)\,h < 0$, i.e. under the condition

$$\Phi \stackrel{\text{def}}{=} -\beta\omega_2 > 0. \tag{38}$$

In that case the spatially homogeneous solutions of (37) given by $A(\tau) = r_0 e^{-i\,h\,r_0^2\tau}$ are exponentially unstable, with maximum growth rate $\sigma_{\max} = |h|r_0^2$.

To analyze the occurrence of MI, one can observe that $\omega(q)$ admits a unique inflection point in the interval $(0, \pi)$, at the wavenumber $q = q_c \in (0, \pi/2)$ satisfying $\cos q_c = v_1(1 - \cos q_c)^2$. In the generic case when $\beta(q_c) \neq 0$, it follows that Φ changes sign at $q = q_c$ (since ω_2 changes sign). Consequently, MI generically occurs for wavenumbers in some interval lying at one side of q_c. This interval may extend or not up to one edge of the phonon band, depending on parameter values. For $q = 0$ (in-phase mode) the condition $\Phi > 0$ reduces to $s < 0$, and for $q = \pi$ (out-of-phase mode) it reduces to $16v_3 + s > 0$ (these conditions have been also obtained in [60] through a Hill's type analysis).

Another important property of the focusing case of the NLS equation (37) is the existence of *sech*-shaped soliton solutions [10]. By the ansatz (36), these solutions yield small amplitude solutions of (6)–(10)–(34) taking the form

$$y_n(t) = \epsilon M \frac{e^{i[qn-(\omega-\epsilon^2\omega''/2)t+\varphi]}}{\cosh[\epsilon(n - c\,t)]} + c.c. + O(\epsilon^{3/2}) \tag{39}$$

on time intervals of length $O(\epsilon^{-2})$, with $M = (-\omega''/h)^{1/2}$. Such solutions therefore correspond to "long-lived" traveling breather excitations of the chain. The existence of exact (permanent) traveling breather excitations close to the form (39) is a delicate question. This result has been proved in special cases for Klein–Gordon lattices (i.e. chains of linearly coupled nonlinear oscillators) and FPU lattices, see [39,56] and references therein. These traveling breather solutions have been obtained as small amplitude homoclinic orbits of an advance-delay differential equation lying on a finite-dimensional center manifold. The homoclinic orbits converge at infinity towards a periodic orbit, whose size can be made exponentially small with respect to the amplitude of the homoclinics, but does not generically vanish. As a result, the traveling breathers can be seen as coherent structures connecting two identical wave trains, whose amplitude can be made exponentially small in ϵ (such waves are called "nanopterons", following the denomination of [32]). Of course, these results do not directly apply to the study of traveling breathers in system (6)–(10)–(34) including both an anharmonic interaction potential and an on-site potential. However, in principle only minor adaptations of the analysis of [56] should be required to prove the same type of results (due to the evenness of W, which preserves the reversibility symmetry of the FPU system used in [56]).

From the above theory, one can draw several differences with respect to the case without precompression studied in Section 3, linked with different features of the NLS and DpS asymptotic limits. Firstly, the anharmonicity parameter s enters the cubic coefficient h of the NLS equation, thereby influencing the focusing or defocusing dynamics of small modulated periodic waves. On the contrary, the DpS equation (12) does not depend on s, as well as the evolution (over long finite times) of small initial data in (6)–(7)–(10). In addition, the profile of (39) becomes loosely localized in the small amplitude limit $\epsilon \to 0$. This is in contrast with the traveling breathers numerically obtained in Section 3.3 in the DpS regime, which are well described by the approximation (12)–(13)–(25), resulting in a constant width in the small amplitude limit. Such differences suggest that the outcome of an impact may be considerably affected by the precompression, and strongly differ from the phenomenology described in Section 3.3. This problem will be numerically examined in the next section.

4.2. Excitation of traveling breathers

In the numerical simulations performed in this section, we fix $d = 1/2$ so that $v_1 \approx 1.06$, $v_2 \approx -0.53$ and $v_3 \approx -0.17$, $q_c \approx 1.17$, and we consider different values of the anharmonicity parameter $s = 1$, $s = 0$ and $s = -1/6$.

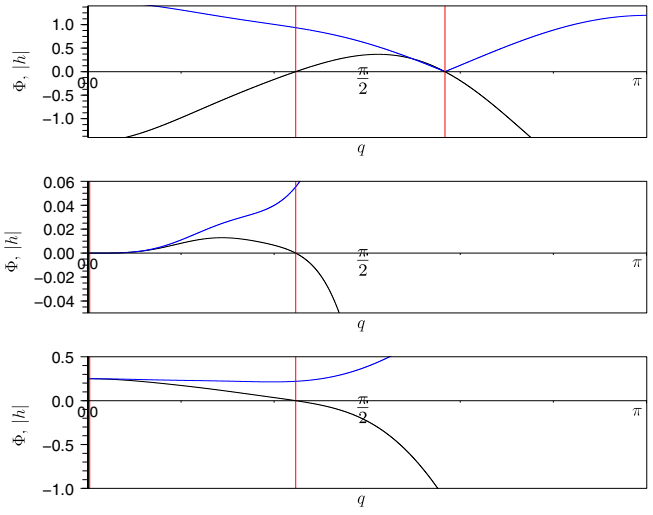

Fig. 24. Graphs of the MI coefficients for different values of s, corresponding to $s = 1$ (top), $s = 0$ (middle) and $s = -1/6$ (bottom). In each panel, the black curve shows the MI coefficient $\Phi(q)$ defined by (38) as a function of wavenumber q. Modulational instability occurs in the bands where $\Phi > 0$, delimited by red lines. The blue curve displays the absolute value $|h(q)|$ of the cubic coefficient of the NLS equation (37), which is proportional (up to a factor depending solely on wave amplitude) to the maximum instability growth rate of the unstable mode with wavenumber q. (For interpretation of the references to colour in this figure legend, the reader is referred to the web version of this article.)

Before analyzing the excitation of the first site of the precompressed chain (and comparing the results to the study of Section 3.3), we illustrate below some features of the MI that will help to interpret the results. For all the above parameter values, there exists a band of unstable phonon modes characterized by $\Phi(q) > 0$ within the NLS approximation. This band and the graph of Φ are shown in Fig. 24. In addition, the graph of $|h(q)|$ indicates the strength of the MI (since the maximum exponential growth rate is proportional to $|h(q)|$ at fixed wave amplitude).

To illustrate the MI phenomenon, we integrate (6)–(10)–(34) numerically for initial conditions

$$\begin{aligned} x_n(0) &= a\sin(qn)(1 + b\cos(2n\pi/N)), \\ \dot{x}_n(0) &= -a\omega\cos(qn)(1 + b\cos(2n\pi/N)) \end{aligned} \tag{40}$$

corresponding to slowly modulated phonons, with $a = 0.15$, $b = 0.01$, a wavenumber q in the band of unstable modes (see Fig. 24), and ω determined by (35). We consider a chain of N particles with periodic boundary conditions. Fig. 25 displays the results for $s = -1/6$, $q = \pi/4$ and $N = 200$. The initial perturbation generates a traveling breather over a long transient (at the end of which a splitting of the pulse occurs). The same phenomenon occurs for $s = 1$ and $s = 0$, albeit the latter case results in slower instabilities and less localized traveling breathers (results not shown).

According to the above computations, long-lived traveling breathers with profiles reminiscent of (39) can be generated from slow modulations of small amplitude unstable phonons, in qualitative agreement with the focusing dynamics of the NLS equation [10]. This raises the question of the excitation of traveling breathers from other types of initial conditions for which a rigorous connection with the NLS equation (such as the results of [30,31]) is not yet available. This problem is examined below for a localized impact. We keep the same values of parameters d, s and integrate (6)–(10)–(34) numerically (for free end boundary conditions), starting from the initial condition (26) with $\dot{y}_1(0) \approx 1.87$. Depending on the value of s, the initial excitation may lead to different dynamical phenomena, and notable differences with respect to the case without precompression are always observed. We shall formally interpret these results in the framework of the

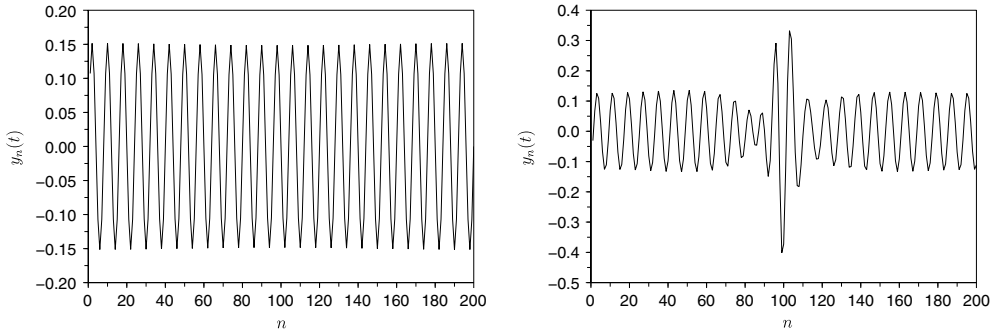

Fig. 25. Evolution of particle positions in the system (6)–(10)–(34) with periodic boundary conditions ($N = 200$ particles). We consider the case $s = -1/6$ with precompression $d = 0.5$. The initial condition (40) is plotted in the left panel (case $q = \pi/4$). Particle displacements plotted at time $t = 6619$ (right panel) reveal the formation of a traveling breather resulting from a modulational instability (the envelope propagates rightwise).

NLS approximation, taking into account different features of the MI depending on s. However, these arguments have to be considered with caution, since the link between the NLS dynamics and the one of the original lattice has been only mathematically established for well-prepared small initial data in [30,31].

The case $s = 1$ is described in Fig. 26, which shows the particle velocity profiles at two different times. The initial perturbation generates a dispersive wave train of substantial amplitude, the edge of which propagates at a velocity close to the maximal group velocity $\omega'(q_c)$. A traveling breather reminiscent of the *sech*-type envelope solitons (39) appears after the impact. It forms around $t = 290$ at the edge of the dispersive wave train, where the linear growth rate of the MI is maximal (since $|h|$ is maximal at $q = q_c$ in the band of unstable modes, see Fig. 24). As expected, the traveling breather is much less localized than the ones previously obtained without precompression (compare Figs. 26 and 22). The "boomerang effect" that occurs without precompression disappears, but a slowing-down of the localized wave still occurs when time increases. As a result, the traveling breather becomes ultimately superposed on an oscillatory tail at both sides of the central pulse, which yields a profile reminiscent of the waves computed in [61] (see also [32,59]). This dynamical behavior is consistent with the "generic" existence of a small non-decaying oscillatory tail propagating with exact traveling breather solutions in standard nonlinear Hamiltonian lattices, as discussed in Section 4.1.

The cases $s = -1/6$ and $s = 0$ yield a different situation described in Fig. 27. The initial localized perturbation generates an important dispersive wave train, and no traveling breather is excited, at least on the time scales of the simulation. The differences with the case $s = 1$ may be formally explained by some qualitative changes in the features of MI. Indeed, for $s = -1/6$ the maximal growth rate of the MI is almost constant among the unstable modes (in contrast with the case $s = 1$), hence none of them becomes dominant during the initial stage of the instability. Moreover, for $s = 0$ one can notice that h is much smaller inside the band of unstable modes. Within the NLS approximation, this implies that the most unstable mode grows around 20 times slower than for $s = 1$, according to the values of $|h(q_c)|$ indicated in Fig. 24. Consequently, MI may not be able to develop significantly at $t \approx 4400$ (Fig. 27). In addition, the range of applicability of the NLS equation is itself questionable, since quintic terms or additional modes may not be negligible due to the smallness of the cubic coefficient h. For $s = -1/6$ and $s = 0$, the modulated wave trains following the main disturbance might be in fact better described by Whitham's equation, as for the dispersive shocks occurring at wavebreaking in hyperbolic continuum limits of Hamiltonian lattices [45,44].

For $s = -1/6$ and $s = 0$, the difference with the case without precompression is again striking since neither a traveling breather nor a surface mode are generated (compare Fig. 27 with Figs. 15, 18 and 20). As a conclusion, according to our results, the precompression attenuates spatial localization, enhances dispersion and modifies the effects of the on-site anharmonicity. These phenomena originate from the additional linear component embedded within the Hertzian interactions, and are partly related to the different properties of the NLS/DpS asymptotic regimes.

5. Conclusion

We have analyzed the properties of discrete breathers in FPU lattices and mixed FPU-Klein–Gordon lattices with Hertzian interactions. While static breathers do not exist in the absence of precompression and of onsite potentials, the addition of the latter creates highly localized breathers, which display a particularly strong mobility, a phenomenon well-described by the DpS equation in the small amplitude regime and associated with the spectral properties (i.e., the pinning mode) of such states. Beyond the DpS limit, we have identified different phenomena depending on the softening or hardening character of the local potential, namely the generation of a surface mode after an impact or the existence of direction-reversing traveling breathers. Importantly also the stability of both the on-site and inter-site breather states obtained was critically dependent on the strength (and sign) of the anharmonicity.

We have also introduced a mechanical model consisting of a chain of stiff cantilevers decorated by spherical beads, which may allow to realize the above localized excitations. According to our study, an impact at one end of the cantilever chain should generate a highly-localized traveling breather. In this regime, contrary to what is the case for a regular cradle under gravity, the ranges of parameters of the problem (e.g., beads of about 1 cm diameter, loads of about 1N, and cantilever width of about 1 cm) are deemed relevant for the observation of such breathers and for the description of the system by the DpS approximation examined herein.

Obviously, one has to stress that the lattice model (33) is simplified and important corrections may apply, in particular to describe the anharmonicity of cantilever bending vibrations, or to take into account possible additional relevant degrees of freedom. In this context, a finite-element modeling would be helpful to validate the model and improve its calibration. In addition, it would be important to take dissipation into account, following e.g. the approach of [62]. Since many sources of dissipation are present (friction, plasticity effects, transmission of vibrational energy through the walls), one may wonder if dissipation may overdamp the dynamics and completely destroy the breathers. However, recent experimental results [16] have demonstrated that static breathers with lifetimes of the order of 10 ms could be generated in diatomic granular chains. During this time, the moving breather computed in Section 3.3.2.2 would travel over approximately 20

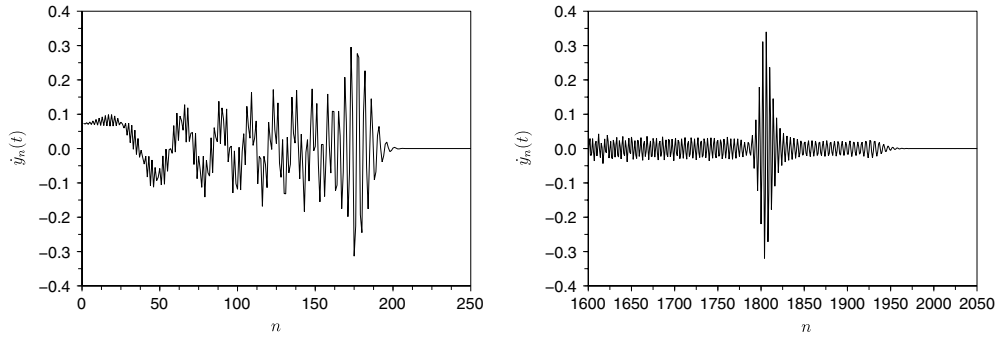

Fig. 26. Snapshot of particle velocities in system (9)–(10)–(34) with anharmonicity parameter $s = 1$ and precompression $d = 0.5$, for the initial condition (26) with $\dot{y}_1(0) \approx 1.87$. The profile is plotted at two different times $t \approx 291$ (left panel), and $t \approx 3000$ (right panel), showing the formation of a traveling breather surrounded by a sizable dispersive wave train.

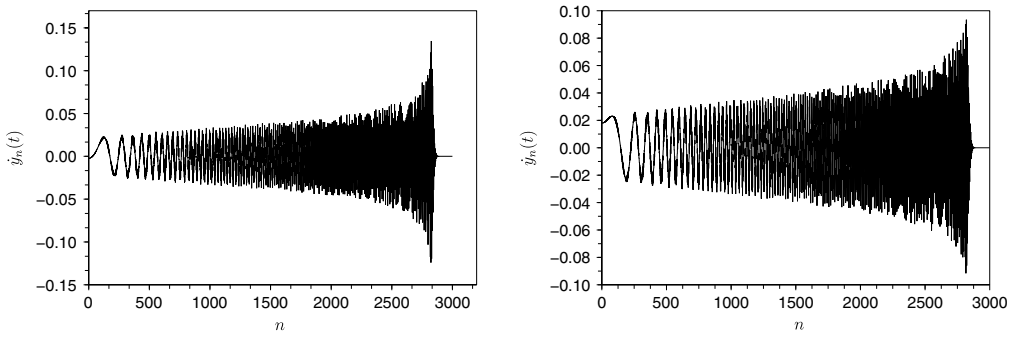

Fig. 27. Same as in Fig. 26, with a snapshot of particle velocities at $t \approx 4399$ for $s = 0$ (left panel) and $s = -1/6$ (right panel).

sites (performing roughly 70 internal oscillations), which would allow for an experimental detection, provided this excitation persists in the presence of dissipation, with moderate changes in velocity and frequency. Although the setting of decorated cantilevers proposed herein would have the additional source of dissipation through radiating energy into the ground (through the clamping of the cantilevers), it is certainly deemed worthwhile to consider such experimental setups and to examine systematically the resulting dynamics.

A different approach which may allow to generate static breathers is linked with modulational instability. Indeed, static breathers have been excited by modulational instabilities in experiments on diatomic granular chains [16], a phenomenon also numerically illustrated in Newton's cradle [21]. In this respect, an extensive study of MI in the cradle model (with the help of the DpS equation) would be of interest. A related aspect concerns the actuation of the system through the driving of a bead with a particular frequency. In fact, the experiments of [16] were realized based on such actuation of the chain at modulationally unstable frequencies rather than the generation of suitable spatially extended, modulationally unstable states. In that regard, it should be noted that it is not straightforward to experimentally initialize desired spatial profiles throughout the lattice in this system.

As we have seen, static breathers may be deformed by weak instabilities resulting in a translational motion and traveling counterparts thereof. However, in an experimental context, these weak instabilities are likely to be irrelevant due to dissipation. To fix the ideas, let us assume a breather lifetime of the order of 10 ms in the presence of dissipation, as in the experiments of [16]. In the computations of Section 3.3.2.2, the breather periods at small amplitude were (roughly) close to 0.15 ms, therefore unstable Floquet eigenvalues $1+\epsilon$ would have an effect over times of order $0.15\epsilon^{-1}$ ms. Consequently, dissipation should destroy the breather well before the instability becomes observable as soon as $\epsilon < 0.015$, and thus the instabilities identified in Section 3.2.2 (where $\epsilon < 10^{-3}$) would be largely dominated by dissipative effects.

On a more theoretical side, an open problem concerns the study of traveling breathers in the absence of precompression. In the above numerical computations, approximate traveling breathers were generated by the dynamics after an impact at one end of the chain. It would be interesting to compute exact traveling breather solutions using the Newton method, as done in references [25,61,59] for other types of lattice models. Motivated by the observation of a small oscillatory tail following the traveling breather in Fig. 14, we expect (as found in the above references) the existence of traveling breathers connecting families of periodic orbits at infinity. In that case, it would be interesting to determine if the minimal amplitude of the oscillatory tails may exactly vanish, as observed in the saturable DNLS equation for particular wave velocities [58,59]. From an analytical point of view, small amplitude traveling breathers bifurcating from the ground state are known to exist in FPU and Klein–Gordon lattices [56,39]. These waves are superposed on a non-decaying oscillatory tail which can be made exponentially small with respect to the breather amplitude. As previously mentioned, they have been obtained as trajectories of an advance-delay differential equation lying on a finite-dimensional center manifold, and homoclinic to a periodic orbit at infinity. Extending this approach to the present case would be very interesting but quite technical, because one should consider center manifolds of periodic traveling waves instead of working near the ground state. This comes from the fact that the dynamical Eq. (9) are fully nonlinear, i.e. their linearization around the trivial state yields uncoupled linear oscillators.

Lastly, the existence (and physical explanation) of direction-reversing traveling breathers remains to be elucidated. Furthermore, it would be relevant to understand in more detail the nature of interactions of the traveling breathers with static defects [54,55] or extended waves [63].

Acknowledgments

Part of this work has been carried out during a visit of P.G.K. to laboratoire Jean Kuntzmann, supported by CNRS, France, to which P.G.K. is grateful for the hospitality. P.G.K. also acknowledges support from the US National Science Foundation through grant CMMI-1000337 and the Alexander S. Onassis Public Benefit Foundation through grant RZG 003/2010-2011 as well as the US AFOSR through grant FA9550-12-1-0332. J.C. acknowledges support from the MICINN project FIS2008-04848. The authors are grateful to the referees for many useful comments. P.G.K. and G.J. wish to thank N. Boechler for helpful inputs on experimental issues. G.J. acknowledges stimulating discussions with B. Bidegaray, E. Dumas, M. Peyrard and G. Theocharis.

References

[1] S. Sen, J. Hong, J. Bang, E. Avalos, R. Doney, Phys. Rep. 462 (2008) 21–66.
[2] F. Fraternali, M.A. Porter, C. Daraio, Optimal design of composite granular protectors, Mech. Adv. Mat. Struct. 17 (2010) 1–19.
[3] A. Spadoni, C. Daraio, Generation and control of sound bullets with a nonlinear acoustic lens, Proc. Natl. Acad. Sci. USA 107 (2010) 7230.
[4] N. Boechler, G. Theocharis, C. Daraio, Bifurcation-based acoustic switching and rectification, Nat. Mater. 10 (2011) 665–668.
[5] V.F. Nesterenko, Dynamics of Heterogeneous Materials, Springer-Verlag, 2001.
[6] E. Falcon, Comportements dynamiques associés au contact de Hertz : processus collectifs de collision et propagation d'ondes solitaires dans les milieux granulaires, Ph.D. thesis, Université Claude Bernard Lyon 1, 1997.
[7] E.J. Hinch, S. Saint-Jean, The fragmentation of a line of ball by an impact, Proc. R. Soc. Lond. Ser. A 455 (1999) 3201–3220.
[8] R.S. MacKay, Solitary waves in a chain of beads under Hertz contact, Phys. Lett. A 251 (1999) 191–192.
[9] M. Porter, C. Daraio, Szelengowicz I., Herbold E.B., Kevrekidis. P.G., Highly nonlinear solitary waves in heterogeneous periodic granular media, Physica D 238 (2009) 666–676.
[10] A.C. Newell, Solitons in Mathematics and Physics, in: CBMS-NSF Regional Conference Series in Applied Mathematics, vol. 48, SIAM, Philadelphia, Pennsylvania, 1985.
[11] J.M. English, R.L. Pego, On the solitary wave pulse in a chain of beads, Proc. Amer. Math. Soc. 133 (6) (2005) 1763–1768.
[12] A. Stefanov, P.G. Kevrekidis, On the existence of solitary traveling waves for generalized Hertzian chains, J. Nonlinear Sci. 22 (2012) 327–349.
[13] H. Hu, A. Strybulevych, J.H. Page, S.E. Skipetrov, B.A. van Tiggelen, Localization of ultrasound in a three-dimensional elastic network, Nat. Phys. 4 (2008) 945.
[14] G. Theocharis, M. Kavousanakis, P.G. Kevrekidis, C. Daraio, M.A. Porter, I.G. Kevrekidis, Localized breathing modes in granular crystals with defects, Phys. Rev. E 80 (2009) 066601.
[15] S. Flach, A. Gorbach, Discrete breathers: advances in theory and applications, Phys. Rep. 467 (2008) 1–116.
[16] N. Boechler, G. Theocharis, S. Job, P.G. Kevrekidis, M.A. Porter, C. Daraio, Discrete breathers in one-dimensional diatomic granular crystals, Phys. Rev. Lett. 104 (2010) 244302.
[17] G. Theocharis, N. Boechler, P.G. Kevrekidis, S. Job, M.A. Porter, C. Daraio, Intrinsic energy localization through discrete gap breathers in one-dimensional diatomic granular crystals, Phys. Rev. E. 82 (2010) 056604.
[18] G. James, P. Noble, Breathers on diatomic Fermi–Pasta–Ulam lattices, Physica D 196 (2004) 124–171.
[19] E. Hascoët, H.J. Herrmann, Shocks in non-loaded bead chains with impurities, Eur. Phys. J. B 14 (2000) 183–190.
[20] S. Job, F. Santibanez, F. Tapia, F. Melo, Wave localization in strongly nonlinear Hertzian chains with mass defect, Phys. Rev. E 80 (2009) 025602(R).
[21] G. James, Nonlinear waves in Newton's cradle and the discrete p-Schrödinger equation, Math. Models Methods Appl. Sci. 21 (2011) 2335–2377.
[22] Y. Starosvetsky, M. Arif Hasan, A.F. Vakakis, L.I. Manevitch, Strongly nonlinear beat phenomena and energy exchanges in weakly coupled granular chains on elastic foundations, SIAM J. Appl. Math. 72 (2012) 337–361.
[23] S. Hutzler, G. Delaney, D. Weaire, F. MacLeod, Rocking Newton's cradle, Amer. J. Phys. 72 (12) (2004) 1508–1516.
[24] A. Pankov, Travelling waves and periodic oscillations in Fermi–Pasta–Ulam lattices, Imperial College Press, London, 2005.
[25] S. Aubry, T. Cretegny, Mobility and reactivity of discrete breathers, Physica D 119 (1998) 34–46.
[26] B. Bidégaray-Fesquet, E. Dumas, G. James, From Newton's cradle to the discrete p-Schrödinger equation, 2013, article (in preparation).
[27] M.I. Molina, R.A. Vincencio, Yu.S. Kivshar, Discrete solitons and nonlinear surface modes in semi-infinite waveguide arrays, Opt. Lett. 31 (2006) 1693–1695.
[28] A. Degasperis, M. Conforti, F. Baronio, S. Wabnitz, Effects of nonlinear wave coupling: accelerated solitons, Eur. Phys. J. Special Topics 147 (2007) 233–252.
[29] M. Johansson, Discrete nonlinear Schrödinger approximation of a mixed Klein–Gordon/Fermi–Pasta–Ulam chain: modulational instability and a statistical condition for creation of thermodynamic breathers, Physica D 216 (2006) 62–70.
[30] J. Giannoulis, A. Mielke, The nonlinear Schrödinger equation as a macroscopic limit for an oscillator chain with cubic nonlinearities, Nonlinearity 17 (2004) 551–565.
[31] J. Giannoulis, A. Mielke, Dispersive evolution of pulses in oscillator chains with general interaction potentials, Discrete Contin. Dyn. Syst. Ser. B 6 (2006) 493–523.
[32] J.P. Boyd, A numerical calculation of a weakly non-local solitary wave: the ϕ^4 breather, Nonlinearity 3 (1990) 177–195.
[33] T. Cretegny, S. Aubry, Spatially inhomogeneous time-periodic propagating waves in anharmonic systems, Phys. Rev. B 55 (1997) 929–932. R11.
[34] T. Dauxois, M. Peyrard, C.R. Willis, Discreteness effects on the formation and propagation of breathers in nonlinear Klein–Gordon equations, Phys. Rev. E 48 (1993) 4768.
[35] R.S. MacKay, J.-A. Sepulchre, Effective Hamiltonian for travelling discrete breathers, J. Phys. A 35 (2002) 3985–4002.
[36] R.S. MacKay, S. Aubry, Proof of existence of breathers for time-reversible or Hamiltonian networks of weakly coupled oscillators, Nonlinearity 7 (1994) 1623–1643.
[37] G. James, J. Cuevas, P.G. Kevrekidis, Breathers and surface modes in oscillator chains with Hertzian interactions, in: Proceedings of the 2012 International Symposium on Nonlinear Theory and its Applications, NOLTA 2012, Palma, Majorca, Spain, 22–26 Oct. 2012, pp. 470–473. Preprint available on arXiv:1301.1769 [nlin.PS].
[38] G. James, B. Sánchez-Rey, J. Cuevas, Breathers in inhomogeneous lattices: an analysis via center manifold reduction, Rev. Math. Phys. 21 (2009) 1–59.
[39] Y. Sire, Travelling breathers in Klein–Gordon lattices as homoclinic orbits to p-tori, J. Dyn. Diff. 7 (2005) 779–823.
[40] P.G. Kevrekidis, The Discrete Nonlinear Schrödinger Equation: Mathematical Analysis, Numerical Computations and Physical Perspectives, Springer-Verlag, Heidelberg, 2009.
[41] J. Cuevas, G. James, P.G. Kevrekidis, B. Malomed, B. Sánchez-Rey, Approximation of solitons in the discrete NLS equation, Journal of Nonlinear Mathematical Physics 15 (supplement 3) (2008) 124–136.
[42] J.L. Marin, S. Aubry, Finite size effects on instabilities of discrete breathers, Physica D 119 (1998) 163–174.
[43] D. Chen, S. Aubry, G.P. Tsironis, Breather mobility in discrete ϕ^4 lattices, Phys. Rev. Lett. 77 (1996) 4776.
[44] M. Herrmann, J.D.M. Rademacher, Riemann solvers and undercompressive shocks of convex FPU chains, Nonlinearity 23 (2010) 277–304.
[45] W. Dreyer, M. Herrmann, Numerical experiments on the modulation theory for the nonlinear atomic chain, Physica D 237 (2008) 255–282.
[46] Q. Dou, J. Cuevas, J.C. Eilbeck, F.M. Russell, Breathers and kinks in a simulated breather experiment, Discrete Contin. Dyn. Syst. Ser. S 4 (2011) 1107–1118.
[47] D.R. Lovett, K.M. Moulding, S. Anketell-Jones, Collisions between elastic bodies: Newton's cradle, Eur. J. Phys. 9 (1988) 323–328.
[48] J. Cuevas, L.Q. English, P.G. Kevrekidis, M. Anderson, Discrete breathers in a forced-damped array of coupled pendula: modeling, computation, and experiment, Phys. Rev. Lett. 102 (2009) 224101.
[49] M. Sato, B.E. Hubbard, A.J. Sievers, Nonlinear energy localization and its manipulation in micromechanical oscillator arrays, Rev. Mod. Phys. 78 (2006) 137–155.
[50] M. Kimura, T. Hikihara, Coupled cantilever array with tunable on-site nonlinearity and observation of localized oscillations, Phys. Lett. A 373 (2009) 1257–1260.
[51] S.C. Green, C.J. Budd, G.W. Hunt, Breathers in a pinned mechanical lattice, SIAM J. Appl. Dyn. Syst. 10 (2011) 66–91.
[52] U. Rabe, K. Janser, W. Arnold, Vibrations of free and surface-coupled atomic force microscope cantilevers: theory and experiments, Rev. Sci. Instrum. 67 (1996) 3281–3293.
[53] L.D. Landau, E.M. Lifshitz, A.M. Kosevich, L.P. Pitaevskii, Theory of Elasticity, Third Edition, in: Theoretical Physics, vol. 7, Butterworth-Heinemann, 1986.
[54] J.J.L. Ting, M. Peyrard, Effective breather trapping mechanism for DNA transcription, Phys. Rev. E 53 (1996) 1011–1020.
[55] J. Cuevas, F. Palmero, J.F.R. Archilla, F.R. Romero, Moving discrete breathers in a Klein–Gordon chain with an impurity, J. Phys. A: Math. Gen. 35 (2002) 10519–10530.
[56] G. Iooss, G. James, Localized waves in nonlinear oscillator chains, Chaos 15 (2005) 015113.
[57] O.F. Oxtoby, I.V. Barashenkov, Moving solitons in the discrete nonlinear Schrödinger equation, Phys. Rev. E 76 (2007) 036603.
[58] T.R.O. Melvin, A.R. Champneys, P.G. Kevrekidis, J. Cuevas, Radiationless traveling waves in saturable nonlinear Schrödinger lattices, Phys. Rev. Lett. 97 (2006) 124101.
[59] T.R.O. Melvin, A.R. Champneys, P.G. Kevrekidis, J. Cuevas, Travelling solitary waves in the discrete Schrödinger equation with saturable nonlinearity: existence, stability and dynamics, Physica D 237 (2008) 551–567.
[60] S. Flach, Tangent bifurcation of band edge plane waves, dynamical symmetry breaking and vibrational localization, Physica D 91 (1996) 223–243.
[61] Y. Sire, G. James, Numerical computation of travelling breathers in Klein–Gordon chains, Physica D 204 (2005) 15–40.
[62] R. Carretero-González, D. Khatri, M.A. Porter, P.G. Kevrekidis, C. Daraio, Dissipative solitary waves in granular crystals, Phys. Rev. Lett. 102 (2009) 024102.
[63] R. Reigada, A. Sarmiento, K. Lindenberg, Energy relaxation in nonlinear one-dimensional lattices, Phys. Rev. E 64 (2001) 066608.